Spectrally resolved four-photon interference of time-frequency-entangled photons

Sofiane Merkouche, Valérian Thiel, and Brian J. Smith

Phys. Rev. A **105**, 023708 — Published 11 February 2022

DOI: 10.1103/PhysRevA.105.023708

Spectrally-resolved four-photon interference of time-frequency entangled photons

Sofiane Merkouche[†],[*] Valérian Thiel,[†] and Brian J. Smith
Department of Physics and Oregon Center for Optical, Molecular, and Quantum Science, University of Oregon, Eugene, Oregon 97403, USA
(Dated: December 15, 2021)

Pairs of photons entangled in their time-frequency degree of freedom are of great interest in quantum optics research and applications, due to their relative ease of generation and their high capacity for encoding information. Here we analyze, both theoretically and experimentally, the behavior of phase-insensitive spectrally-resolved interferences arising from two pairs of time-frequency entangled photons. At its core, this is a multimode entanglement swapping experiment, whereby a spectrally resolved joint measurement on the idler photons from both pairs results in projecting the signal photons onto a Bell state whose form depends on the measurement outcome. Using this scheme we herald a large, though non-orthogonal, set of pulse-mode Bell states, which we characterize through spectral measurements and through two-photon quantum interference. In principle, the number of mutually-orthogonal states which can be generated with our scheme is limited only by the amount of entanglement available in the sources, and thus our setup demonstrates a versatile and scalable multimode entanglement swapping scheme requiring no source engineering.

I. INTRODUCTION

With the advent of the quantum information age, it is well-established by now that the encoding of quantum information into the degrees of freedom of light is the key component of quantum communication networks [1]. Whereas polarization and spatial-mode encoding benefit from ease of implementation, they are prone to scrambling from environmental noise and optical-fiber transmission, which undermines their suitability for long-distance communication. Meanwhile, the time-frequency (TF) degree of freedom is more robust in this regard (frequency-channel crosstalk does not occur in optical fiber), and TF-encoding has now been established as a complete toolkit for quantum-information processing [2], opening an active venue of research into the generation, manipulation, and measurement of TF-encoded quantum states of light.

In the quantum regime, entanglement plays a key role in many protocols for computation [3] and communication [4, 5]. Furthermore, entanglement of photons has recently been of great interest to the metrology and spectroscopy communities due to its promise of enhancements in sensitivity beyond what is attainable in the classical domain [6]. It comes as no surprise, then, that the generation of photon pairs in well-defined TF-entangled states is a widely-researched area of quantum optics, and great strides have been made over this terrain in the past two decades [7]. In addition to state generation, harnessing the full capabilities of quantum entanglement also requires the ability to perform projective measurements onto entangled states. Indeed, entangled measurements [8], of which the Bell-state measurement is the prototype, are nearly as ubiquitous in quantum protocols as entangled states, most notably in quantum teleportation [9] and entanglement swapping [10].

In this work, we describe theoretically, and demonstrate experimentally, an entanglement swapping scheme that relies on the multimode nature of TF-entanglement in pairs of photons. The central component of the setup is a multimode, frequency-resolved Bell-state measurement (BSM), performed on idler photons from two independent TF-entangled pairs generated from spontaneous parametric down conversion (SPDC). The BSM heralds the signal photons onto a pulsed Bell state whose central frequencies depend on the result of the BSM. In this way we are able to herald multiple orthogonal Bell pairs and verify entanglement in each pair, all derived from the same source state and within the measurement scheme. This aspect of our work can be viewed as a generalization of pulse-mode entanglement swapping, such as that reported in Ref. [11], to utilizing the high-dimensional TF entanglement that is available in standard of-the-shelf SPDC sources. In section II we outline the theory underlying our work. In section III we describe the experimental setup. Then, in section IV we describe our results, which show remarkable agreement with a simple and intuitive Gaussian model using pure quantum states, before concluding in section V. Finally, in the Appendix we cover the more technical details of our work which would otherwise encumber the account of our main results.

II. THEORY

A. Four photon state

The entanglement swapping protocol we realize is depicted conceptually in Fig. 1. The protocol consists of two independent spontaneous parametric down conversion (SPDC) sources. Each source generates pairs of photons into paths labeled by the bosonic operators $\hat{a}_n$ for

[*] Corresponding author: oqt@uoregon.edu
[†] These authors contributed equally to the work.

the signal and $\hat{b}_n$ for the idler, where $n \in \{1, 2\}$ labels the two sources. Here we consider pulsed collinear type II SPDC sources, where the signal and idler modes are distinguished by their orthogonal polarization. Furthermore, all the light is collected into single-mode optical fibers, so that only the time-frequency degree of freedom is relevant.

In Appendix A, we derive the general four-photon quantum state of SPDC in the context of Fig. 1. Generally, this state is a coherent superposition containing terms corresponding to either source generating two pairs of photons, as well as a term corresponding to each source generating exactly one pair of photons. This last term is the one of interest throughout this work, and in Appendix A we outline the assumptions that allow us to consider solely this term. Under the assumptions that both sources are identical, the four photon state arising from this term is given by

$$|\psi\rangle = \int \mathrm{d}^4\omega \; f(\omega_\mathrm{S}, \omega_\mathrm{I}) f(\omega'_\mathrm{S}, \omega'_\mathrm{I}) \times \hat{a}_1^\dagger(\omega_\mathrm{S}) \hat{b}_1^\dagger(\omega_\mathrm{I}) \hat{a}_2^\dagger(\omega'_\mathrm{S}) \hat{b}_2^\dagger(\omega'_\mathrm{I}) \, |\mathrm{vac}\rangle \,, \tag{1}$$

where $f(\omega_\mathrm{S}, \omega_\mathrm{I})$ is the joint spectral amplitude (JSA) associated with either source. The modulus squared of the JSA, known as the joint spectral intensity (JSI), corresponds to the probability density function for creating a pair of photons, called signal and idler, at optical frequencies ω_S and ω_I, respectively. The two-photon state from either source contains spectral entanglement when the JSA cannot be factored into a product of the form $f(\omega_\mathrm{S}, \omega_\mathrm{I}) = f_\mathrm{S}(\omega_\mathrm{S}) f_\mathrm{I}(\omega_\mathrm{I})$.

Most of the experiments in this paper rely on performing a spectrally-resolved BSM on the idler photons. Although the spectral resolution of this BSM is finite, we model the results in the limit of narrow spectral resolution. This limit has the benefit of providing a simple and intuitive model with which to understand the physics in terms of pure quantum states. A more complete model taking into account the finite spectral resolution of the BSM and the resulting states is then easily constructed from this pure-state approximation, which is done in Appendix B. As we shall see, the pure-state approximation is sufficient to account for the majority of the results of our experiment.

B. Heralded state and JSI

A Bell-state measurement is performed on the idler photons by resolving their frequencies at the output of a 50:50 beam splitter, with a small path difference at the input giving a relative time delay τ_I as depicted in Fig. 1. The beam splitter transforms the input field operators

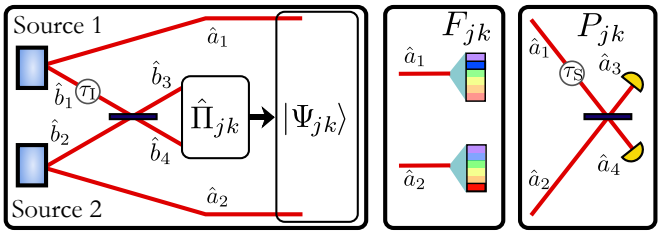

FIG. 1. Conceptual scheme of the experiment. Two sources, 1 and 2, emit photon pairs into the modes labelled $\hat{a}$ and $\hat{b}$ for signal and idler, respectively. The BSM $\hat{\Pi}_{jk}$ on the idler photons projects the signal photons onto the state $|\Psi_{jk}\rangle$. This state in the signal modes is characterized by measuring its JSI F_{jk}, as well as the two-photon interference signal P_{jk}. The time delays τ_I and τ_S serve to balance the interferometer.

$\hat{b}_1^\dagger$, $\hat{b}_2^\dagger$ into

$$\begin{aligned} \hat{b}_3^\dagger(\Omega) &= \frac{e^{i\Omega\tau_\mathrm{I}} \hat{b}_1^\dagger(\Omega) + \hat{b}_2^\dagger(\Omega)}{\sqrt{2}}, \\ \hat{b}_4^\dagger(\Omega') &= \frac{e^{i\Omega'\tau_\mathrm{I}} \hat{b}_1^\dagger(\Omega') - \hat{b}_2^\dagger(\Omega')}{\sqrt{2}}, \end{aligned} \tag{2}$$

and coincidences are detected between $\hat{b}_3$ and $\hat{b}_4$. For clarity, we will label the optical frequencies of the idlers as Ω and those of the signals as ω. Because we use the pure state approximation, we can consider that this spectral measurement is achieved with perfect resolution, whereby the measurement operator is given by

$$\hat{\Pi}_{jk} = \hat{b}_3^\dagger(\Omega_j) \hat{b}_4^\dagger(\Omega_k) \, |\mathrm{vac}\rangle \langle \mathrm{vac}| \, \hat{b}_3(\Omega_j) \hat{b}_4(\Omega_k) \tag{3}$$

which is a projector onto single photon states with monochromatic frequencies Ω_j and Ω_k. Although this limit of frequency-resolved detection corresponds to projective measurements, it is important to recognize that a more realistic model of the measurement with finite resolution should incorporate a positive operator-valued measure (POVM) element defined over a frequency band, as we outline in Appendix B. Furthermore, since the POVM formalism describes the most general quantum measurements, projectors such as $\hat{\Pi}_{jk}$ are indeed POVM elements, and for consistency throughout the text, we refer to all our measurement operators as POVM elements. We define

$$|\Omega_j, \Omega_k\rangle_{34} = \hat{b}_3^\dagger(\Omega_j) \hat{b}_4^\dagger(\Omega_k) \, |\mathrm{vac}\rangle \,,$$

and we compute the heralded signal state, $|\Psi_{jk}\rangle_{12}$, defined by

$$|\Psi_{jk}\rangle_{12} \otimes |\Omega_j, \Omega_k\rangle_{34} = \frac{\hat{\Pi}_{jk} \, |\psi\rangle}{\sqrt{p_{jk}}}, \tag{4}$$

with the norm p_{jk} given by

$$p_{jk} = \langle \psi | \, \hat{\Pi}_{jk} \, |\psi\rangle \,. \tag{5}$$

Since our original state $|\psi\rangle$ only contains a single photon in each of paths $\hat{b}_1^\dagger$ or $\hat{b}_2^\dagger$, applying $\hat{\Pi}_{jk}$ acts as an effective Bell-state measurement on these modes. Henceforth, we will drop the 12-index in $|\Psi_{jk}\rangle_{12}$ for convenience.

To compute the form of $|\Psi_{jk}\rangle$, we will introduce, for convenience, the reduced density matrices for the states of the signal and idler photons, given respectively by,

$$\begin{aligned}\rho_{\mathrm{S}}(\omega,\omega') &= \int \mathrm{d}\Omega f(\omega,\Omega) f^*(\omega',\Omega),\\ \rho_{\mathrm{I}}(\Omega,\Omega') &= \int \mathrm{d}\omega f(\omega,\Omega) f^*(\omega,\Omega'),\end{aligned} \tag{6}$$

both of which obey the relation $\rho(\omega,\omega') = \rho^*(\omega',\omega)$. Using these, along with the assumption of identical sources, it is straightforward to show that

$$p_{jk} = \frac{1}{2}\Big[\rho_{\mathrm{I}}(\Omega_j,\Omega_j)\rho_{\mathrm{I}}(\Omega_k,\Omega_k) - |\rho_{\mathrm{I}}(\Omega_j,\Omega_k)|^2\cos\theta_{jk}\Big], \tag{7}$$

with

$$\theta_{jk} = (\Omega_j - \Omega_k)\tau_{\mathrm{I}} = \Delta\Omega_{jk}\tau_{\mathrm{I}}, \tag{8}$$

where we defined $\Delta\Omega_{jk}$ as the difference between the heralding frequencies. Eq. (7) is the probability distribution for a coincidence between the idler photons at (Ω_j,Ω_k), or equivalently, the JSI of the idler photons at the output of the beam splitter.

Most importantly, the heralded signal Bell-state has the simple form

$$|\Psi_{jk}\rangle = \frac{|\phi_j\rangle_1|\phi_k\rangle_2 - e^{i\theta_{jk}}|\phi_k\rangle_1|\phi_j\rangle_2}{\sqrt{2\mathcal{C}_{jk}}}, \tag{9}$$

where $|\phi_j\rangle_n$ is a pulse-mode normalized single photon state [12] given by

$$|\phi_j\rangle_n = \int \mathrm{d}\omega\, \phi_j(\omega)\hat{a}_n^\dagger(\omega)|\mathrm{vac}\rangle, \tag{10}$$

with

$$\phi_j(\omega) = \frac{f(\omega,\Omega_j)}{\sqrt{N_j}}, \tag{11}$$

where $N_j = \rho_{\mathrm{I}}(\Omega_j,\Omega_j)$, as described in Appendix H, and $n\in\{1,2\}$. Essentially, $|\phi_j\rangle_n$ is the state that the signal photon is projected onto, when its corresponding idler photon is detected at frequency Ω_j. Finally the normalization constant $\mathcal{C}_{jk}$ is given by

$$\mathcal{C}_{jk} = 1 - |\langle\phi_j|\phi_k\rangle|^2\cos\theta_{jk}, \tag{12}$$

where the inner product $\langle\phi_j|\phi_k\rangle$ is taken either in mode 1 or in mode 2, but we have dropped the index for better readability. The functions ϕ_j are defined from the JSA and several identities are shown in Appendix H. While normalized, they are not necessarily orthogonal, hence the dependence on the modal overlap in the normalization from Eq. (12). In Sec.IV, we will use a Gaussian approximation that gives a simple expression for those functions.

Since nearly all of our measurements are conditioned upon the BSM on the idler photons, we will use the state $|\Psi_{jk}\rangle$ to calculate our quantities of interest. In addition, we also consider the case of a non-resolving BSM, given by

$$\begin{aligned}\hat{\Pi} &= \sum_{j,k}\hat{\Pi}_{jk}\\ &= \iint \mathrm{d}\Omega_j\mathrm{d}\Omega_k\,|\Omega_j,\Omega_k\rangle\langle\Omega_j,\Omega_k|,\end{aligned} \tag{13}$$

which, upon taking $\mathrm{Tr}\Big(\hat{\Pi}|\psi\rangle\langle\psi|\Big)$, heralds the mixed state

$$\hat{\rho} = \frac{\sum_{jk} p_{jk}|\Psi_{jk}\rangle\langle\Psi_{jk}|}{\sum_{jk} p_{jk}}. \tag{14}$$

This state is normalized by $\sum_{jk} p_{jk}$, which is not equal to unity in general, but this fact is inconsequential to our measurements, as only the relative probabilities p_{jk} are physically relevant. At this point we note that we are using the sum $\sum_{jk}$ in place of the integral $\int \mathrm{d}\Omega_j\mathrm{d}\Omega_k$. This summation serves as a reminder that the pure state description of $|\Psi_{jk}\rangle$ is itself an approximation stemming from the infinite spectral resolution limit. In Appendix B we justify the validity of this approximation, which gives similar results as the model taking into account the finite resolution of the BSM and the resultant impurity of the heralded state.

C. State characterization and entanglement verification

We characterize the heralded state $|\Psi_{jk}\rangle$ first by measuring its joint spectral intensity (JSI). This measurement is defined by the POVM element

$$\hat{\Pi}^{\mathrm{JSI}} = |\omega_1,\omega_2\rangle\langle\omega_1,\omega_2|, \tag{15}$$

with

$$|\omega_1,\omega_2\rangle = \hat{a}_1^\dagger(\omega_1)\hat{a}_2^\dagger(\omega_2)|\mathrm{vac}\rangle,$$

and we calculate the resultant JSI as

$$F_{jk}(\omega_1,\omega_2) = \langle\Psi_{jk}|\hat{\Pi}^{\mathrm{JSI}}|\Psi_{jk}\rangle. \tag{16}$$

Using (9), we then obtain

$$F_{jk}(\omega_1,\omega_2) = \frac{1}{2\mathcal{C}_{jk}}\Big|\phi_j(\omega_1)\phi_k(\omega_2) - e^{i\theta_{jk}}\phi_j(\omega_2)\phi_k(\omega_1)\Big|^2. \tag{17}$$

In the absence of spectral resolution in the BSM, the heralded state is $\hat{\rho}$ from Eq.(14), and the measured JSI is given by

$$F(\omega_1,\omega_2) = \sum_{jk} p_{jk} F_{jk}(\omega_1,\omega_2). \tag{18}$$

In terms of previously defined quantities, this function takes the general form

$$F(\omega_1,\omega_2) = \frac{1}{2}\Bigg[\rho_{\mathrm{S}}(\omega_1,\omega_1)\rho_{\mathrm{S}}(\omega_2,\omega_2) - \left|\int \mathrm{d}\Omega f(\omega_1,\Omega) f^*(\omega_2,\Omega) e^{i\Omega\tau_{\mathrm{I}}}\right|^2\Bigg]. \tag{19}$$

To verify that the heralded state $|\Psi_{jk}\rangle$ is indeed entangled, beyond classical correlation, two-photon interference is used in a manner analogous to Refs. [11, 13]. In our verification protocol, the signal photons are combined at a 50:50 beam splitter while scanning a relative delay between the input modes ($\hat{a}_1$ and $\hat{a}_2$) denoted by τ_{S} and monitoring coincidences at the output modes ($\hat{a}_3$ and $\hat{a}_4$) as depicted in Fig. 1. These modes transform as

$$\begin{aligned}\hat{a}_3^\dagger(\omega) &= \frac{e^{i\omega\tau_{\mathrm{S}}}\hat{a}_1^\dagger(\omega) + \hat{a}_2^\dagger(\omega)}{\sqrt{2}},\\ \hat{a}_4^\dagger(\omega') &= \frac{e^{i\omega'\tau_{\mathrm{S}}}\hat{a}_1^\dagger(\omega') - \hat{a}_2^\dagger(\omega')}{\sqrt{2}}.\end{aligned} \tag{20}$$

The POVM element associated with such a coincidence detection is defined as

$$\hat{\Pi}_{\mathrm{verif}} = \iint \mathrm{d}\omega\mathrm{d}\omega' \,|\omega,\omega'\rangle\langle\omega,\omega'|\,, \tag{21}$$

with

$$|\omega,\omega'\rangle = \hat{a}_3^\dagger(\omega)\hat{a}_4^\dagger(\omega')\,|\mathrm{vac}\rangle\,, \tag{22}$$

where we will again consider only the terms that contain both $\hat{a}_1^\dagger$ and $\hat{a}_2^\dagger$. The probability of detecting a coincidence heralded for the input state $|\Psi_{jk}\rangle$ is given by

$$\begin{aligned}P_{jk}(\tau_{\mathrm{S}}) &= \left\langle \Psi_{jk}\right| \hat{\Pi}_{\mathrm{verif}} \left|\Psi_{jk}\right\rangle\\ &= \iint \mathrm{d}\omega\mathrm{d}\omega' \left|\langle\omega,\omega'|\Psi_{jk}\rangle\right|^2.\end{aligned} \tag{23}$$

Evaluating this using Eq. (9), we obtain

$$\begin{aligned}P_{jk}(\tau_{\mathrm{S}}) = \frac{1}{2\mathcal{C}_{jk}}\Big(&1\\ &+ \Phi_j(\tau_{\mathrm{S}})\Phi_k(\tau_{\mathrm{S}})\cos\left[(\omega_j-\omega_k)\tau_{\mathrm{S}} - \theta_{jk}\right]\\ &- \mathcal{O}(|\langle\phi_j|\phi_k\rangle|^2)\Big).\end{aligned} \tag{24}$$

where $\Phi_j(\tau_{\mathrm{S}})$ is modulus of the Fourier transform of $|\phi_j(\omega)|^2$, ω_j is the center frequency of ϕ_j, and finally,

$$\begin{aligned}\mathcal{O}(|\langle\phi_j|\phi_k\rangle|^2) = &\left|\int \mathrm{d}\omega \phi_j^*(\omega)\phi_k(\omega)e^{i\omega\tau_{\mathrm{S}}}\right|^2\\ &+ |\langle\phi_j|\phi_k\rangle|^2\cos\theta_{jk}\end{aligned} \tag{25}$$

are terms that depend on the overlap of ϕ_j and ϕ_k and are negligible except for when $\Omega_j \approx \Omega_k$, which is the regime where $p_{jk} \approx 0$. The main feature of $P_{jk}(\tau_{\mathrm{S}})$ is the interference due to the oscillating term at the difference frequency $(\omega_j - \omega_k)$. This interference is a signature of frequency-bin entanglement [13, 14], as it arises due to the coherence between the two terms in the state $|\Psi_{jk}\rangle$. It is important to note that $P_{jk}(\tau_{\mathrm{S}})$ also depends on τ_{I} implicitly through θ_{jk}, and we will sometimes write $P_{jk}(\tau_{\mathrm{S}},\tau_{\mathrm{I}})$ when showing this dependence explicitly.

In the absence of frequency resolution of the BSM, we can consider the interference signal associated with the mixed state $\hat{\rho}$, and obtain

$$P(\tau_{\mathrm{S}},\tau_{\mathrm{I}}) = \sum_{jk} p_{jk} P_{jk}(\tau_{\mathrm{S}},\tau_{\mathrm{I}}). \tag{26}$$

In terms of the previously defined quantities, we have

$$\begin{aligned}P(\tau_{\mathrm{S}},\tau_{\mathrm{I}}) = \frac{1}{4}\Bigg(1 &+ \left|\iint \mathrm{d}\omega\mathrm{d}\Omega\ |f(\omega,\Omega)|^2\, e^{i(\omega\tau_{\mathrm{S}}+\Omega\tau_{\mathrm{I}})}\right|^2\\ &- \iint \mathrm{d}^2\Omega\ |\rho_{\mathrm{I}}(\Omega,\Omega')|^2\, e^{i(\Omega-\Omega')\tau_{\mathrm{I}}}\\ &- \iint \mathrm{d}^2\omega\ |\rho_{\mathrm{S}}(\omega,\omega')|^2\, e^{i(\omega-\omega')\tau_{\mathrm{S}}}\Bigg).\end{aligned} \tag{27}$$

In both Eqs. (18) and (26), we see that the quantities F and P are obtained by taking a weighted sum over the individual quantities F_{jk} and P_{jk}, with the weights given by p_{jk}. The results are equivalent to replacing the spectrometers with "bucket" (non-resolving) detectors. This weighted sum may also be interpreted in terms of probabilities, where the probability of obtaining a four fold coincidence is the product of the probability of a heralding event from a coincidence between the idler photons, and the probability of a coincidence between the signal photons conditional on the heralding event. This concept of weighting the average is analogous to other experiments that utilize multi-pixel detection in the spatial [15] or spectral [16, 17] domains.

III. EXPERIMENT

A. Description

The experimental setup shown in Fig. 2(a) consists of a single 2.5mm-long bulk BiBO crystal, double-passed by a pump laser to generate two pairs of SPDC photons in a type-II configuration, where signal and idler are orthogonally polarized. By convention we label the first-pass SPDC process as source 1, and the second-pass process as source 2. The pump for this process is obtained by second harmonic generation (SHG) of a commercial Ti:Sapph laser (Spectra-Physics Tsunami) delivering 100 fs-long pulses at a repetition rate of 80 MHz centered at a wavelength of 830 nm. A part of the Ti:Sapph beam

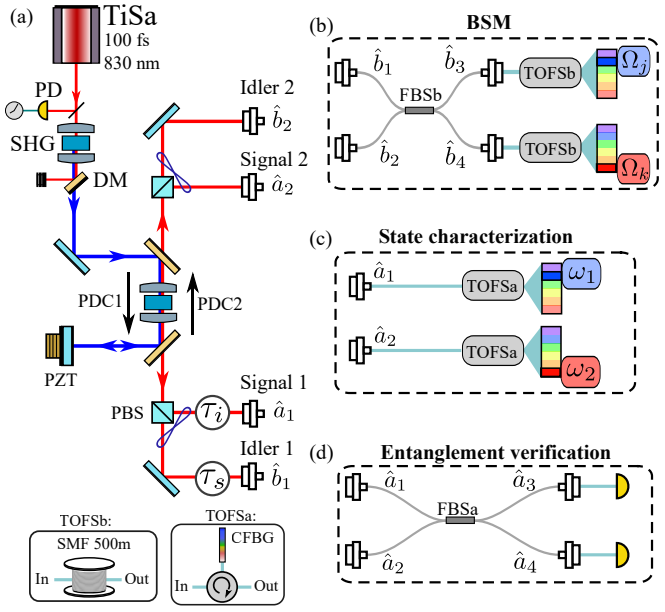

FIG. 2. a) Experimental setup; PD: photodiode; SHG: second harmonic generation; DM: dichroic mirror; PDC: parametric down conversion; PZT: piezoelectric actuator; PBS: polarizing beamsplitter; TOFS: time of flight spectrometer; SMF: single mode fiber; CFBG: chirped fiber Bragg grating; FBS: fiber beam splitter. b) Bell state measurement: the idler photons interferences are spectrally-resolved and used as a herald. c-d) different configuration of the measurement on the signal photons depending on the experiment.

is directed to a fast photodiode to generate a clock for the experiment. The SHG is realized in a 1mm-long type I BiBO crystal and the output consist of another train of pulse centered at 415 nm with a bandwidth of 2.3 nm at full width at half-maximum (FWHM). The SHG efficiency is over 30%, with an average output power of over 300 mW at 415 nm. To ensure better quality of the spatial mode of the SPDC photons, the pump beam is spatially filtered by a pinhole, transmitting about 60% of the power. This filtering has been shown to greatly optimize the heralding efficiency of SPDC sources when the photons are collected by single-mode fibers.

The double-pass configuration consists of reflecting the pump beam back into the crystal, while transmitting the SPDC single photons from the first source (first pass) through the dichroic mirrors used to steer the pump beam. This configuration ensures spectral overlap of the two sources. The back mirror for the second source (second pass) is mounted on a piezo actuator (PZT) with a 10 μm travel to finely adjust the phase between the two sources. The SPDC photon pairs are separated by polarization with polarizing beam splitter (PBS) as signal (V polarization, 10 nm FWHM) and idler (H polarization, 16 nm FWHM) and injected into single mode polarization-maintaining fibers. Motorized delay lines are introduced into both signal and idler of source 1 to match their time of arrival with the other photons from the second source.

The BSM is achieved by interfering the idler photons from each source on a fiber beamsplitter prior to the heralding spectral measurement. Spectral resolution is then obtained by utilizing frequency-to-time conversion at the output of the beamsplitter, thus heralding the frequency bins Ω_j and Ω_k, see Fig. 2(b). Finally, the heralded JSI and verification is done respectively by routing the signal photons through the setup described in Fig. 2(c), (d).

B. Detection

The single photons are detected utilizing superconducting nanowire single photon detectors (SNSPDs) from IDQuantique (ID281) which can detect the arrival time of photons with a resolution of 20 ps. This temporal resolution is translated into spectral resolution using time-of-flight spectrometers (TOFS), thanks to frequency-to-time conversion [18, 19]. For coarse spectral resolution, we used two spools of 500 m-long HP780 fiber (see Fig. 2(a)). These imprint a dispersion of approximately 50 ps per nm of bandwidth at 830 nm, with losses of less than 1 dB per spool. For fine resolution, we used two chirped fiber Bragg gratings (CFBG from Teraxion) with a dispersion of $\sim$ 1000 ps/nm [20] (see Fig. 2(a)). This extra resolution comes at the expense of an overall signal attenuation of over 10 dB due to coupling losses and to a finite spectral window of 10 nm. The photocurrent coming out of the detectors is registered with a time-to-digital converter (TDC, ID900 from IDQuantique). The time reference is provided by the optical clock, thus ensuring that each time tag is taken with respect to a stable signal for each pulse.

When the photons are detected at the SNSPDs, their time of arrival is recorded with an adjustable precision. Throughout this work, this resolution was set to 100 ps unless stated otherwise, which corresponds to a spectral resolution that depends on which dispersive medium is used. Using the calibration data shown in Fig. 14 in Appendix C, this spectral resolution is 0.1 nm for the CFBG and 2 nm for the fiber spools. These resolutions define the minimal bin size in which the frequency of any event is recorded. Therefore, when doing any type of four-fold coincidence measurement, the time of arrival of every event may be binned with that resolution in a histogram, thus resulting in spectral bins, or pixels, as depicted in Fig. 3, which can be analyzed in post processing.

For instance, for experiments that only require spectral resolution on the herald (such as the verification P_{jk}), time tags corresponding to heralding frequencies Ω_j, Ω_k are acquired and subsequently binned at the resolution of the spectrometer, corresponding to the probability of getting spectral coincidences in every possible combination of frequency bins. When all four spectrometers are needed (for instance to measure the JSI F_{jk} heralded by a BSM at frequencies Ω_j and Ω_k), the measurement then

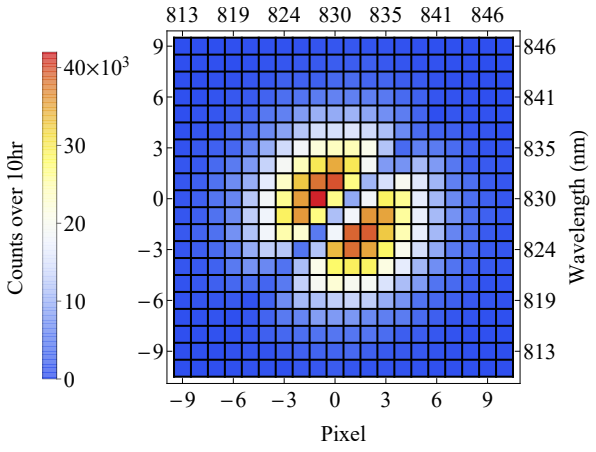

FIG. 3. Acquisiton of the heralded JSI p_{jk} of the idler photons showing the calibration and indexing convention of the frequency bins.

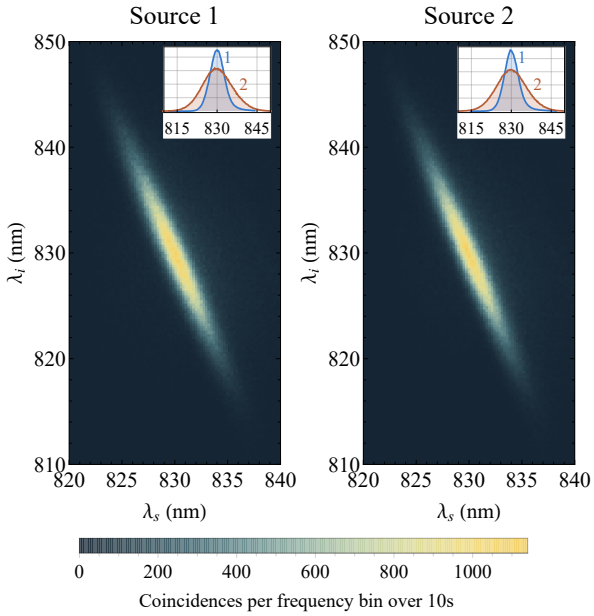

FIG. 4. Experimental joint spectral intensity of both sources. Insets: marginal spectra.

consists of four sets of time tags that can be binned into a four-dimensional histogram, such as shown in Fig. 6. For more readability, we label those heralding bins by integers j and k, such that index 0 corresponds to Ω_0, the central wavelength of the idler spectrum. The axes in Fig. 3 give the index-to-wavelength mapping.

C. Source distinguishability

This experiment relies on the indinstinguishability of the two sources as noted in the previous section. This has to be achieved on every degree of freedom. Since the polarization and the spatial degree of freedom are constrained by polarization-maintaining fibers, there remains to match the sources in frequency and in time.

The spectral indistinguishability can be estimated by measuring the joint spectral intensity of both sources. We obtained such JSI measurements by using the two 500m fiber spools (TOFSb) to detect signal and idler photons from each source in coincidence, while operating the time tagger at its maximum resolution of 13 ps, such that the spectral resolution is only limited by the timing jitter of the SNSPDs. These measurements are shown in Fig. 4. It can be seen that both sources are very similar thanks to the dual-pass configuration of the pump. A Gaussian fit to this experimental JSI is used throughout this paper to define the parameters of the JSA $f(\omega, \Omega)$ that are used in our mathematical model, as described in Sec.IV A. Note that there can be an additional cause of distinguishability due to spectral phase mismatch between both sources which cannot be determined with an intensity measurement. Therefore, the dispersion was mostly matched in every path of the interferometer by ensuring that every fiber element had the same length.

Temporal mode matching is achieved by scanning both delays τ_S and τ_I while monitoring the coincidences between ports $\hat{b}_3$ and $\hat{b}_4$ for the idlers (at FBSb) and $\hat{a}_3$ and $\hat{a}_4$ for the signals (at FBSa), which do not share photon number correlations. This results in an unheralded Hong-Ou-Mandel (HOM) dip with a poor visibility (less than 10%), which is still sufficient to coarsely match the time of arrival of the photons. We also measured a higher-visibility HOM interference in a heralded manner by detecting fourfold coincidences between ports $\hat{b}_1$, $\hat{b}_2$, $\hat{a}_3$ and $\hat{a}_4$. In Appendix E, we show how such a measurement with and without spectral resolution can give a lower bound on the purity of the heralded state.

Finally, another convenient method [21] to match both sources can be applied. With the configuration from Fig.1, we can monitor the two-fold coincidences between combinations of one output from each beamsplitter, for instance $\hat{b}_3$ and $\hat{a}_3$. When both delays are matched, i.e. $\tau_S = \tau_I = 0$, then these coincidences oscillate at the optical frequency. This interference is phase-sensitive, and analogous to classical first-order interference, except that it is observed in the coincidences. In Appendix D, we show that the visibility of this interference provides a direct measurement of the overlap between both sources, taking into account any phase effects. This method proved essential to accurately match delays before every experiment, while it also provided a bound to quantify indistinguishability, with a maximum measured contrast of 80%.

IV. SIMULATIONS AND RESULTS

In this section, we further model the experiment with a Gaussian approximation of the JSA to derive analytical expressions from the quantities defined in Sec. II. This al-

lows for a better understanding of the dependence of the interferences on the experimental parameters, notably on the delay between the idler photons in the BSM. We then compare our experimental results to the theory using this approximation.

A. Gaussian model

It is convenient to write the JSA $f(\omega_S, \omega_I)$ as a Gaussian distribution by approximating the sinc function with a Gaussian of the same width :

$$f(\omega_S,\omega_I) = C\,\exp\left[-\left(\frac{\omega_S-\omega_0}{2\sigma_S}\right)^2-\left(\frac{\omega_I-\omega_0}{2\sigma_I}\right)^2 - \alpha(\omega_S-\omega_0)(\omega_I-\omega_0)\right], \quad (28)$$

where σ_s (σ_I) is the cross-sectional width of the JSI in the ω_S- (ω_I-) direction evaluated at ω_I (ω_S), ω_0 is the center frequency, α quantifies the amount of spectral entanglement, and $C = \left(\int \mathrm{d}^2\omega\,|f(\omega,\omega')|^2\right)^{-1/2}$ is a normalization constant. Fitting the experimental JSI from Fig. 4 to this function, we obtain the following parameters: $\sigma_S = 2.39$ THz, $\sigma_I = 5.24$ THz and $\alpha = 37.5\cdot 10^3$ fs^2. These provide all the values necessary to simulate the experiment in the Gaussian model that is presented here. Note that the center frequency ω_0 is adjusted to the experimental data, so it is a free parameter.

Using the form of Eq. (28) for the JSA, the density matrices ρ_S and ρ_I are given by

$$\rho_S(\omega,\omega') = C^2\sqrt{2\pi}\sigma_I\exp\left[-\frac{(\omega-\omega_0)^2+(\omega'-\omega_0)^2}{4\sigma_S^2} + \frac{1}{2}\alpha^2\sigma_I^2(\omega+\omega'-2\omega_0)^2\right], \quad (29)$$

$$\rho_I(\Omega,\Omega') = C^2\sqrt{2\pi}\sigma_S\exp\left[-\frac{(\Omega-\omega_0)^2+(\Omega'-\omega_0)^2}{4\sigma_I^2} + \frac{1}{2}\alpha^2\sigma_S^2(\Omega+\Omega'-2\omega_0)^2\right]. \quad (30)$$

Meanwhile, the ϕ_j functions are given by

$$\phi_j(\omega) = \frac{1}{\sqrt{\sigma_S\sqrt{2\pi}}}\exp[-(\omega-\omega_j)^2/4\sigma_S^2], \quad (31)$$

which are Gaussians with a width equal to that of the signal's cross-sectional width and a central frequency given by

$$\omega_j - \omega_0 = -2\alpha\ \sigma_S^2\ (\Omega_j-\omega_0). \quad (32)$$

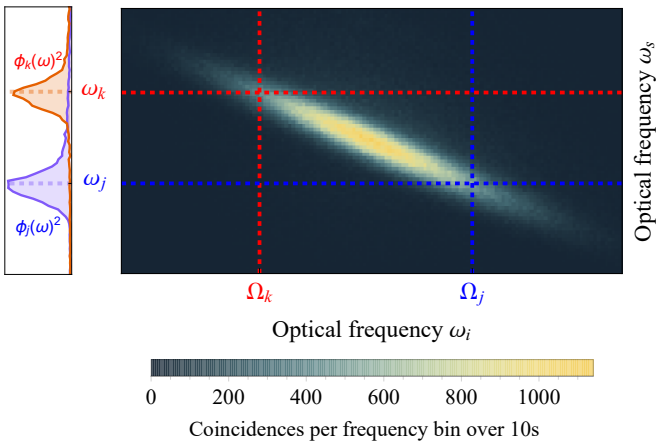

FIG. 5. Gaussian approximation of the spectral heralding: a detection at frequency $\Omega_{j(k)}$ projects the signal photon onto the mode $\phi_{j(k)}$, centered at $\omega_{j(k)}$, shown on the left (dashed). The pure state model assumes that the idler photon is detected with perfect resolution onto a mode with infinitesimal spectral support (top, dashed). A more accurate development is shown in Appendix B, which considers integration over a finite spectral window for the herald.

Finally, the normalization constant $\mathcal{C}_{jk}$ is given by

$$\mathcal{C}_{jk} = 1 - \exp\left[-\Delta\omega_{jk}^2/4\sigma_S^2\right]\cos\left[\Delta\Omega_{jk}\tau_I\right], \quad (33)$$

where $\Delta\omega_{jk} = \omega_j - \omega_k$ is the difference between the central frequencies of the heralded modes, and follows the relation $\Delta\omega_{jk} = -2\alpha\sigma_s^2\Delta\Omega_{jk}$. Note that, for most of our data, $(\omega_j-\omega_k)^2 \gg \sigma_S^2$, so that $\mathcal{C}_{jk} \simeq 1$. In Fig. 5, we used the experimental JSI to plot the measured $\left|\phi_{j(k)}(\omega)\right|^2$ in the limit of infinite spectral resolution at the BSM.

In the following, we first consider the case of a perfect BSM with $\tau_I = 0$, and then explore the effect of minor distinguishability in the BSM with $\tau_I \neq 0$. The latter, more general, case, not only describes the four photon interference effect more comprehensively, but also allows for the heralding of the generalized Bell states given by Eq. (9).

B. Case of $\tau_I = 0$ ($\theta_{jk} = 0$)

We first study the case where the idler paths are exactly matched, setting $\tau_I = 0 (\theta_{jk} = 0)$, which yields the results that we report on in [22]. Under this constraint, and using the Gaussian model in Eq. (28), we proceed to obtain analytic forms for our measured quantities. First, the probability p_{jk} of performing a BSM at frequencies Ω_j and Ω_k and heralding the state $|\Psi_{jk}\rangle$ is given by Eq. (7) with $\theta_{jk} = 0$

$$p_{jk} = \frac{1}{2}\left[\rho_I(\Omega_j,\Omega_j)\rho_I(\Omega_k,\Omega_k) - |\rho_I(\Omega_j,\Omega_k)|^2\right]. \quad (34)$$

The distribution p_{jk} in fact corresponds to the joint probability of detecting two photons at the output of a beam

splitter, when they are in a separable state at the input, with each photon described by a density matrix ρ_{I}. Notably, the indistinguishability of the photons manifests as a dip along the degenerate $\Omega_j = \Omega_k$ frequencies as $p_{j=k} = 0$. This implies that the probability of measuring any quantities is zero in this case. An experimental measurement of p_{jk} is shown in Fig. 3, showing the bimodal structure of this distribution. It also shows our labelling convention for $\Omega_{j(k)}$ where we set $j(k) = 0$ to correspond to Ω_0 which is the center frequency of the degenerate SPDC light.

Next we compute the JSI F_{jk} associated with the state $|\Psi_{jk}\rangle$ from Eq. (17)

$$F_{jk}(\omega_1, \omega_2) = \frac{\left|\phi_j(\omega_1)\phi_k(\omega_2) - \phi_j(\omega_2)\phi_k(\omega_1)\right|^2}{2\mathcal{C}_{jk}}, \quad (35)$$

which can be approximated for $|\Omega_j - \Omega_k| \gg 0$, *i.e.* for distant heralding frequencies, as

$$F_{jk}(\omega_1, \omega_2) \simeq \frac{|\phi_j(\omega_1)\phi_k(\omega_2)|^2 + |\phi_j(\omega_2)\phi_k(\omega_1)|^2}{2}, \quad (36)$$

which corresponds to two Gaussian spots centered at (ω_j, ω_k) and (ω_k, ω_j), mirror-symmetric about the $\omega_1 = \omega_2$ axis. For exactly degenerate heralding events $\Omega_j = \Omega_k$, the heralded JSI vanishes as the probability of obtaining a BSM result is null in this case.

In the intermediate case where $\Omega_j \simeq \Omega_k$, the two Gaussian spots of the heralded JSI begin to overlap. However, the cross terms obtained by expanding Eq. (35) manifest in the JSI as a dip along the degenerate $\omega_1 = \omega_2$ frequencies, akin to Eq. (34). The heralded JSI is simulated in Fig. 6(a) for the pure state approximation and using values of (Ω_j, Ω_k) that are determined experimentally, showing the aforementioned behavior. To retrieve the same quantity experimentally, we set up the experiment for the characterization procedure (Fig. 2(c)) and measure spectral coincidences at the output of FBSa heralded by a BSM at frequencies (Ω_j,Ω_k) (Fig. 2(b)). The result is shown in Fig. 6(b) where the frequency bins are labelled according to Fig. 3. Note that both color maps are normalized, such that the amount of energy per bin has to be multiplied by the probability of realizing this measurement, given by p_{jk} in Fig. 3. Therefore, when computing the total number of four fold coincidences per pixel in Fig. 6(b), we obtain exactly the distribution depicted in Fig. 3.

We assess the validity of our theoretical model by comparing it with the experimental data. For each measured F_{jk}, the counts are distributed into two clusters. We calculate the center of mass of each of the two clusters for a given experimental F_{jk}, and, by taking the difference of the centers of mass, obtain an experimental measure of $\Delta\omega_{jk}$ for that JSI. We compute the relative error with respect to the theoretical value of each $\Delta\omega_{jk}$ from the Gaussian model as given by Eq. (32). Over the whole set presented in Fig. 6(b), the relative error is 25%, which is mostly dominated by the statistical noise due to the low number of events close to the degenerate heralding frequencies ($j = k$). For the F_{jk} with a high number of total counts (corresponding to a high probability of a coincidence between the heralding photons, see Fig. 3), the relative error is lower than 10%. This simple comparison shows that the pure state approximation used in our model is adequate for describing our results.

Taking a weighted sum over $F_{jk}(\omega_1, \omega_2)$ from Eq. (35), with the weights given by p_{jk} according to Eq. (18), we obtain the mixed-state JSI $F(\omega_1, \omega_2)$ from Eq. (19) with $\tau_{\mathrm{I}} = 0$, which simplifies to

$$F(\omega_1, \omega_2) = \frac{1}{2}\left[\rho_{\mathrm{S}}(\omega_1, \omega_1)\rho_{\mathrm{S}}(\omega_2, \omega_2) - |\rho_{\mathrm{S}}(\omega_1, \omega_2)|^2\right]. \quad (37)$$

First we note that the distribution $F(\omega_1, \omega_2)$ for the signal photons is analogous to the distribution p_{jk} from Eq. (34) for the idler photons. Indeed, this is the joint spectral distribution that would be obtained were the beam splitter placed in the signal paths rather than the idler paths, and the fact that such a distribution is measured without the presence of a beam splitter is evidence of the non-local nature of this fourfold measurement. In Fig. 7(a), we simulate $F(\omega_1, \omega_2)$ using the values obtained from the source JSI's, where it can be seen the bimodal structure persists in the summation.

By summing our experimental data from Fig. 6(b) over all heralded bins, we obtain the histogram shown in Fig. 7(b), which closely matches the simulation. We note that the JSI is indeed zero for degenerate frequencies, which is a consequence of HOM interference. The measurement of the heralded JSI shows the validity of the pure state approximation for the resolution of the heralding TOFS, which is sufficiently narrow.

We now proceed to evaluate the entanglement verification signal $P_{jk}(\tau_{\mathrm{S}})$ from Eq. (24), for this case of $\theta_{jk} = 0$. We find that $\Phi_j(\tau_{\mathrm{S}}) = \Phi_k(\tau_{\mathrm{S}})$ since the Gaussians $\phi_{j(k)}$ only differ in their first moment $\omega_{j(k)}$ (see Eqs. (31) and (32)), such that we have:

$$P_{jk}(\tau_{\mathrm{S}}) = \frac{1}{2\mathcal{C}_{jk}}\Big\{1 + e^{-\sigma_{\mathrm{S}}^2\tau_{\mathrm{S}}^2}\cos\left[\Delta\omega_{jk}\tau_{\mathrm{S}}\right] - |\langle\phi_j|\phi_k\rangle|^2(1 + e^{-\sigma_{\mathrm{S}}^2\tau_{\mathrm{S}}^2})\Big\}. \quad (38)$$

Similar to the heralded JSI, we analyzing this function depending on the spectral distance between Ω_j and Ω_k. We find that for $|\Omega_j - \Omega_k| \gg 1/\alpha\sigma_S$, $\langle\phi_j|\phi_k\rangle \to 0$ such that the verification signal reduces to

$$P_{jk}(\tau_{\mathrm{S}}) = \frac{1 + e^{-\sigma_{\mathrm{S}}^2\tau_{\mathrm{S}}^2}\cos\left[\Delta\omega_{jk}\tau_{\mathrm{S}}\right]}{2}. \quad (39)$$

The constant term corresponds to a background probability of 1/2 of getting a coincidence event between uncorrelated, heralded single photons after the balanced beam splitter. The other term is a Gaussian envelope with the transform-limited temporal width of the signal photon, analogous to what is obtained in classical

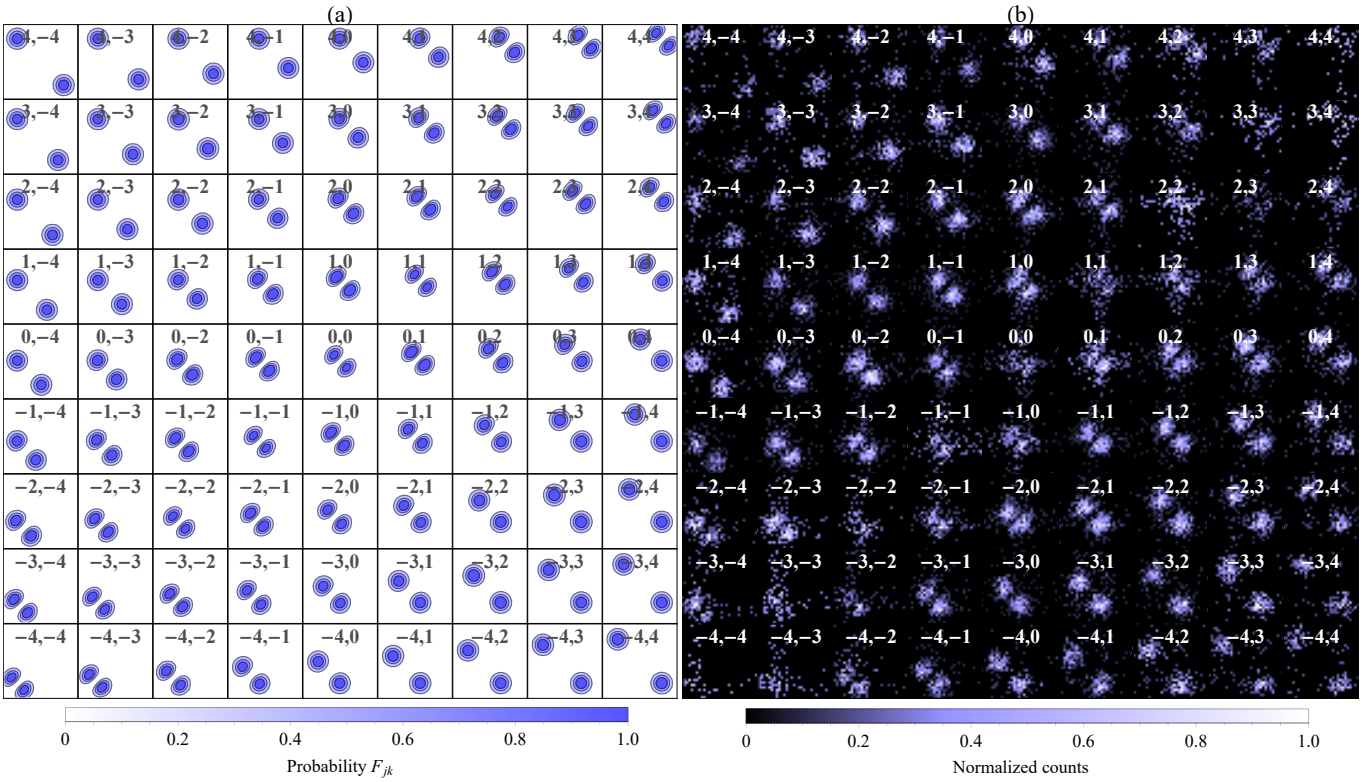

FIG. 6. (a) Simulation of the heralded JSI F_{jk} for pure states, from Eq. (35), using experimental parameters derived from the sources' JSI measurement. (b) Experimental result from [22] obtained by acquiring 30000 spectral coincidences over 10 hours and binning the JSI into frequency bins, labelled according to Fig. 3.

cross-correlation between ultrafast pulses. This envelope is modulated by fringes at the difference of the heralded frequencies $\omega_j - \omega_k$. Note that the fringes vanish when setting $\alpha = 0$ in Eq. (32), consistent with the notion that the observed fringes are a result of discrete frequency entanglement. Additionally, for the case of $\tau_\mathrm{I} = 0$ and $\theta_{jk} = 0$, these fringes have no phase offset and always a maximum at $\tau_\mathrm{S} = 0$.

In the pure state model, the probability p_{jk} of obtaining a coincidence detection event after the balanced beam splitter at degenerate frequencies $\Omega_j = \Omega_k$ is null, and the verification signal Eq. (38) is not defined. However, we find that it has the following limit

$$P_{j\to k}(\tau_\mathrm{S}) \to \frac{1}{2} - \frac{1}{2}\left(2\sigma_\mathrm{S}^2\tau_\mathrm{S}^2 - 1\right)e^{-\sigma_\mathrm{S}^2\tau_\mathrm{S}^2}, \qquad (40)$$

which can be easily demonstrated by noticing that $\langle\phi_j|\phi_k\rangle$ is a Gaussian function of the variable $\Delta\omega_{jk}$ under the Gaussian approximation (see for instance Eq. (33)). The expression is similar to that reported in [11] that utilizes an engineered non-linear interaction to obtain spectral Bell states.

In Fig. 8(a), we plotted the simulated P_{jk} using our approximated model and parameters obtained experimentally. This plot shows the previously described behavior, showing oscillations at the difference frequency which merge into a single peak in the near degenerate case. The

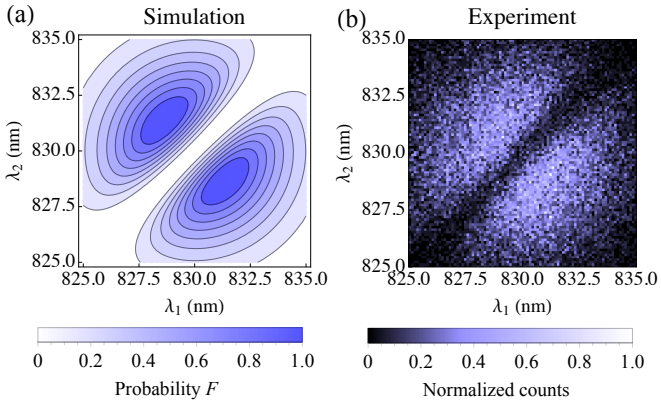

FIG. 7. (a) Simulation of the full heralded JSI F defined by the sum of Eq. (18) over all j, k. (b) Experimental result obtained by summing the acquisitions from Fig. 6(b) over all bins.

background color map for these plots represent the probability of measuring these events, *i.e.* p_{jk} from Eq. (34).

In Fig. 8(b), we show the experimental counterpart, with the colored background representing the experimental p_{jk} obtained by computing the total number of counts in each bin. Using a fit to the Gaussian model (shown as a solid red curve in the experimental plot), we again

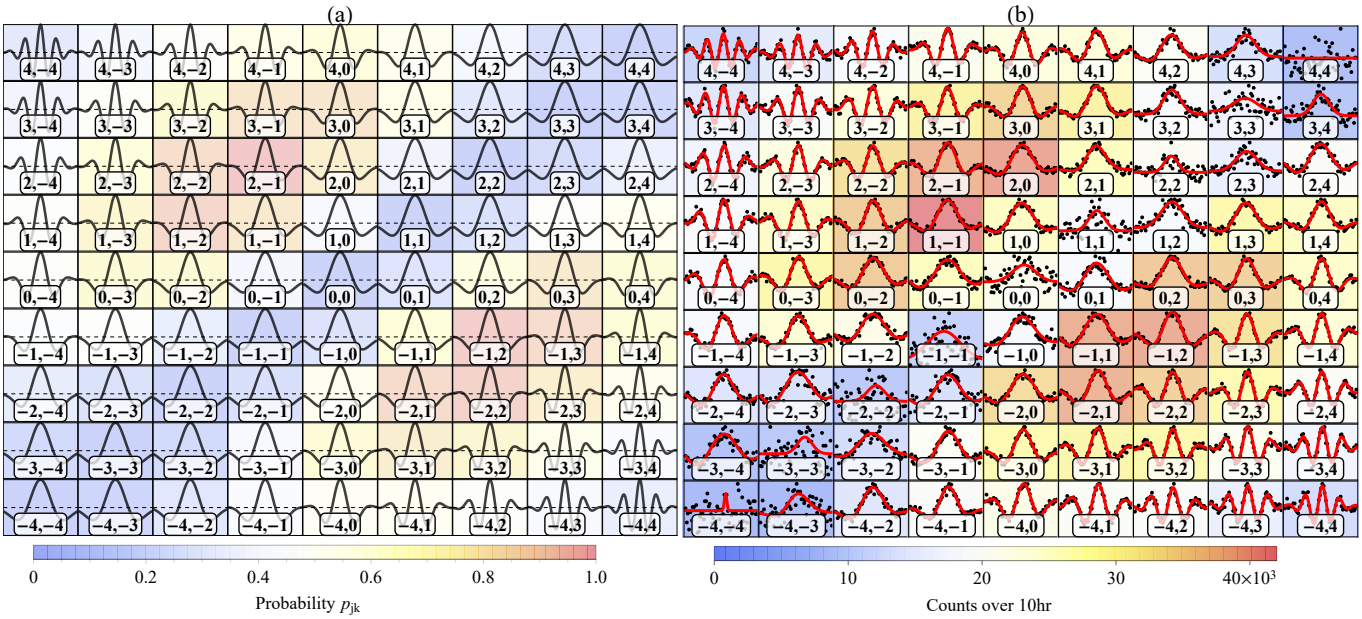

FIG. 8. Left: simulation of the entanglement verification signal P_{jk} for pure states, see Eq. (38). Right: experimental result from [22], obtained by binning the verification signal acquired over 15 hours. These results are fitted to the approximated model from (39). The frequency bins are labelled according to Fig. 3. The colormap in the background represents the probability p_{jk} of an heralding event, theoretical (left) and experimental (right).

assess the validity of the model. The fitted parameters $\Delta\omega_{jk}$ are within 15% of the value predicted by the model when averaged over all bins, while for several bins that contain faster oscillations (such as $(3,-3)$ and its immediate neighbors), the relative error is lower than 5%. It is also worth noting that the fitted values agree within the same margins with the retrieved values from the experimental JSI in Fig.6(b). Additionally, we find that the visibility of the interference fringes is between 70 and 80%. While the visibility should in theory be unity, in practice it is limited by the indistinguishability of the two source JSA's. In App. D, we demonstrate this relationship and we experimentally estimate the indistinguishability to be on the order of 80%, and thus the visibility of the fringes shown in Fig. 8(b) is in good agreement with the theory (a).

Finally we evaluate the verification signal $P(\tau_S)$ with $\theta_{jk}=0$ for the non-spectrally-resolved case, given by Eq. (26). We find that it contains four terms:

$$P(\tau_S)=\frac{1}{4}\Bigg[1+\left|\iint \mathrm{d}\omega\mathrm{d}\Omega\ |f(\omega,\Omega)|^2\, e^{i\omega\tau_S}\right|^2 - \iint \mathrm{d}^2\Omega\ |\rho_I(\Omega,\Omega')|^2 - \iint \mathrm{d}^2\omega\ |\rho_S(\omega,\omega')|^2\, e^{i(\omega-\omega')\tau_S}\Bigg]. \quad (41)$$

The first term is simply a background probability, while the second term corresponds to the overlap between the two sources with a relative delay τ_S between the signal photons. Evaluating this term reveals a Gaussian along τ_S whose width depends on the joint temporal distribution of the sources. This is quite similar to the cross-correlation between two classical pulses, except that in the present case, the phase of the fringes is constant, implying that the P_{jk} sum coherently to a single peak at $\tau_S=0$. We will see in the next section how that phase can be offset by introducing an additional time delay in the BSM.

The last two terms of Eq. (41) correspond respectively to the overlap integrals between the idler and the signal density matrices of each source. The former evaluates to a constant, which is unity when the sources are perfectly matched. The latter describes an unheralded HOM dip between the signal photons. Hence, the full verification signal can be summarized as a Gaussian peak centered in a HOM dip which is similar in form to Eq. (40). In Fig. 9(a), we plot a simulation of the full signal $P(\tau_S)$ showing this behavior. In Fig. 9(b), we show the experimental result obtained without binning the data from Fig. 8(b), where the red curve is not a fit, but rather the sum of the fits to the individual P_{jk} signals. Most remarkably, the visibility of the HOM peak is not limited by the purity of the incident quantum state, suggesting that antibunching can reveal entanglement even for a certain class of mixed states.

We stress that the presence of oscillating fringes in $P_{jk}(\tau_S)$ or a peak in $P(\tau_S)$, where the coincidence probability goes above the baseline of 1/2, is a witness of an entangled state (see, for example, [14]). Our setup is therefore capable of performing entanglement swapping between a large number of frequency Bell states. As we

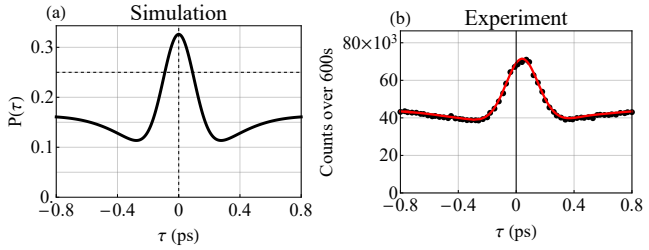

FIG. 9. Probability $P(\tau_S)$ of a coincidence heralded by a BSM without spectral resolution. Left: simulation from Eq. (41); Right: experimental result presented in [22] obtained by summing the individual P_{jk} that are depicted in Fig. 8(b). The solid red curve is a sum of the individual fits on the experimental Gaussian model from Eq. (39).

show in [22], not all of the heralded states shown in Fig. 6(b) are mutually orthogonal, but it is possible to select multiple subsets which form a set of mutually orthogonal Bell states. In Appendix G, we show how to post-select an orthogonal set of states by running an algorithm that isolates sets of quasi-orthogonal modes, all of which satisfy the verification procedure for our entanglement swapping protocol.

C. Case of $\tau_I \neq 0$ ($\theta_{jk} \neq 0$)

We now study the case when there is a temporal delay τ_I between the idler photons at the output of FBSb. Note that when this delay becomes too large compared to the temporal width $\sigma_I^{-1} \approx 300$ fs of the idler photons, they become distinguishable at the output of the beam splitter, effectively reducing the entanglement in the heralded Bell state. Therefore, in the scope of the paper, we take τ_I to be smaller than this value, such that the state $|\Psi_{jk}\rangle$ retains some entanglement. One limitation of the pure state model arises because the idler BSM from Eq. (3) assumes perfect spectral resolution, leading to infinite temporal support of the quantities defined in Sec. II over τ_I whereas they should necessarily be bounded by an envelope whose width is inversely proportional to the spectral resolution. The derivation for the mixed state case, corresponding to finite spectral resolution, is shown in Appendix B. Nevertheless, the pure state model accurately predicts our results and is therefore sufficient to describe the effects of slight distinguishability in the BSM.

The heralded state in the Gaussian model is given by Eq.(9) and shows a phase offset between the two states that depends on τ_I. The heralded JSI from Eq. (17) evaluates to

$$F_{jk}(\omega_1,\omega_2) = \frac{1}{2\mathcal{C}_{jk}}\Big[\,|\phi_j(\omega_1)\phi_k(\omega_2)|^2 + |\phi_k(\omega_1)\phi_j(\omega_2)|^2 - 2\gamma_{jk}(\omega_1,\omega_2)\cos\left(\Delta\Omega_{jk}\tau_I\right)\Big], \quad (42)$$

where $\gamma(\omega_1,\omega_2) = \phi_j(\omega_1)\phi_k(\omega_2)\phi_j(\omega_2)\phi_k(\omega_1)$ for real modes $\phi_{j(k)}$, for simplicity. The last term is responsible for the HOM dip along the degenerate frequencies $\omega_1 = \omega_2$, marking indistinguishability. As previously, $\gamma_{jk} \to 0$ when heralding distant bins $|\Omega_j - \Omega_k| \gg 0$ so the delay between the idlers photons has no influence. However, for degenerate bins $\Omega_j \to \Omega_k$ and for $\tau_I < \sigma_I^{-1}$, $\gamma_{jk} \times \cos\theta_{jk} \to 0$ which causes the two Gaussian spots to merge.

Putting these limits together, we find that a small delay between the idler photons results in a heralded JSI similar to Fig. 6(a) where the JSI in the bins close to the $j \to k$ diagonal are more or less merged depending on τ_I. For spectral bins that are spaced further, the JSI is unchanged since the distinguishability is marked by a relative phase between the Gaussian spots.

The full JSI is obtained by summing F_{jk} according to Eq.(18):

$$F(\omega_1,\omega_2) = \frac{\rho_S(\omega_1,\omega_1)\rho_S(\omega_2,\omega_2) - \Gamma(\omega_1,\omega_2;\tau_I)}{2}, \quad (43)$$

where Γ is a function that depends on the overlap of the signal density matrices as a function of the idler delay (see Appendix H). Similar to the previous case, the overlap between ϕ_j and ϕ_k depends on the indistinguishably in time of the idlers.

We next consider the entanglement verification signal from Eq. (24), which depends on both τ_S and τ_I. Evaluating it with the Gaussian model, we obtain

$$P_{jk}(\tau_S,\tau_I) = \frac{1}{2\mathcal{C}_{jk}}\Big(1 + e^{-\sigma_S^2\tau_S^2}\cos\left[\Delta\omega_{jk}\tau_S - \theta_{jk}\right] - |\,\langle\phi_j|\phi_k\rangle\,|^2(e^{-\sigma_S^2\tau_S^2} + \cos\theta_{jk})\Big). \quad (44)$$

We perform yet another asymptotic behavior analysis. For distant heralding frequencies, we find that the limit is similar to Eq. (39) with an additional phase shift

$$P_{jk}(\tau_S,\tau_I) = \frac{1 + e^{-\sigma_S^2\tau_S^2}\cos\left[\Delta\omega_{jk}(\tau_S - \tau_I')\right]}{2}, \quad (45)$$

where we used Eq. (32) to factorize by the difference of heralded frequencies and we defined $\tau_I' = \tau_I/2\alpha\sigma_S^2$. We can see that the value of τ_I has a more noticeable effect compared to the heralded JSI. The fringes are no longer synchronized to the envelope and a phase shift occurs when the delay between the idlers photons is nonzero. This effect is quite important in our case since a delay as small as 100 fs between the idler photons is sufficient to cause a phase shift of π due to the relatively large spectral bandwidth of the JSA. Note that using the more realistic mixed state model, the envelope of the fringes is also affected by this delay and causes a reduction in visibility. In the pure state approximation, the envelope in the idler direction is infinite, but it is sufficient to show the most noticeable effect of the phase shift. Note also that it is possible to find a value for both delays such that

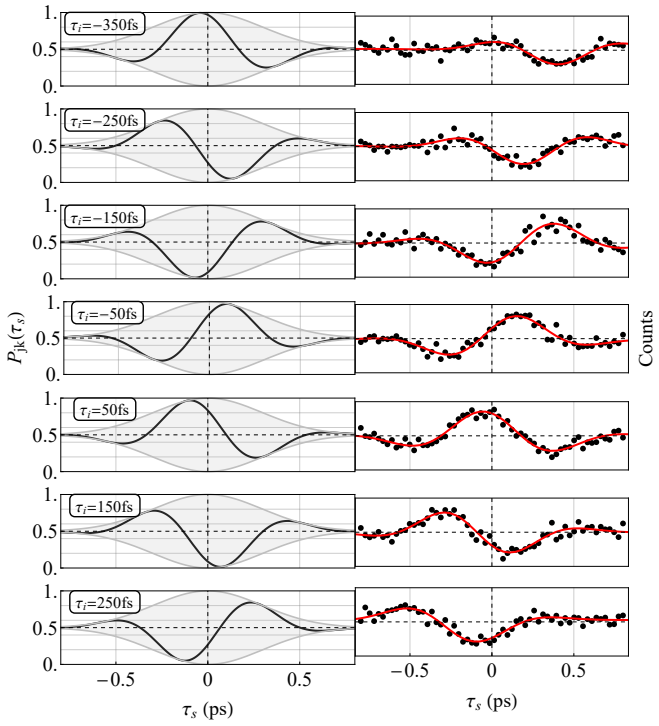

FIG. 10. Simulated (left) and experimental (right) probability to get a coincidence at FBSa between $\hat{a}_3$ and $\hat{a}_4$ heralded by a BSM at frequencies Ω_j and Ω_k for $(j,k) = (2,-2)$. The simulation utilizes the Gaussian, pure state approximation from Eq. (45) with the same parameters as in the experimental case. The experimental plots are acquired over 900s for different positions of the idler stage (on the right). The heralding frequencies are separated by 8nm (or about 10 THz). The red curve represents a fit to the theoretical model. This is a different representation of the data shown in Fig. 11 in the bin labelled $(2,-2)$.

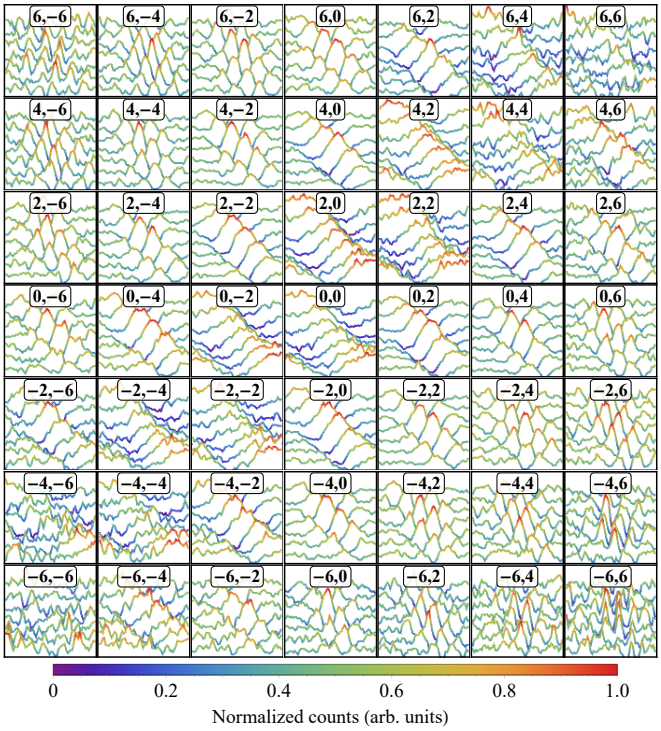

FIG. 11. Waterfall plot of P_{jk} plotted against τ_S (horizontal) for different values of τ_I (vertical) where each plot represents a frequency bin Ω_j, Ω_k labelled by j and k. The plot range and units for τ_S and τ_I are the same as shown in Fig. 10. For each j,k subplot, the color gradient spans the entire range for that subplot, such that the color is representative of the amount of data collected.

$\tau_S = \tau_I'$, in which case the phase shift cancels, but the visibility of the fringes would be decreased. This is illustrated in Fig. 10 which compares a simulation (left) that uses the approximated model with the same parameters as the experimental results (right). The entanglement verification utilizes the previous experimental protocol for 7 different values of τ_I. While we see good qualitative good agreement between the experimental and simulated fringes, the envelope in the model has no dependence on τ_I whereas it is clearly the case experimentally.

For near-degenerate heralding frequencies, we have the following limit

$$P_{j\to k}(\tau_S,\tau_I) = \frac{1}{2} - \frac{1}{2}\cdot\frac{2\sigma_S^2(\tau_S-\tau_I')^2-1}{1+4(\tau_I')^2}e^{-\sigma_S^2\tau_S^2}. \quad (46)$$

which is equal to Eq. (40) when setting $\tau_I = 0$. Putting both limits together, we find that a scan over τ_S and τ_I of the verification signal P_{jk} from Eq. (44) look very similar to Fig. 8(a), except that the fringes will be offset as a function of τ_I while the peak close to the diagonal remains centered. In both cases, the visibility is decreased.

This effect was very useful experimentally to verify that the delay at both beam splitters was as close to zero as possible. Moreover, the decrease in contrast for non-zero values of τ_I is yet another proof that the visibility of the oscillations in P_{jk} is a marker of entanglement. In Fig. 11 we show an experimental waterfall plot representing each P_{jk} for values of τ_I ranging from -300 to +300 fs which originates from the same dataset as Fig. 10. In this measurement, the spectrally resolved heralding is done at half the resolution than used earlier (shown in Fig. 3) to have sufficient data statistics. These plots show that the fringes have a phase shift as a function of τ_I for distant (j,k) frequency bins as predicted by Eq. (45), while in the degenerate $j = k$ case, the fringes collapse to a single peak as described by Eq. (46). The phase shift is defined by the proportionality factor between τ_I and τ_I', which depends on the amount of entanglement and on the spectral bandwidth of the signal photons. This data shows that entanglement swapping is still achieved for this specific range of delay mismatch in the BSM, even though this mismatch introduces some distinguishability.

Finally, by repeating the same experiment either without spectral resolution of the BSM or by summing the individual P_{jk} according to Eq. (26), we find that the expression of the verification signal is then given by

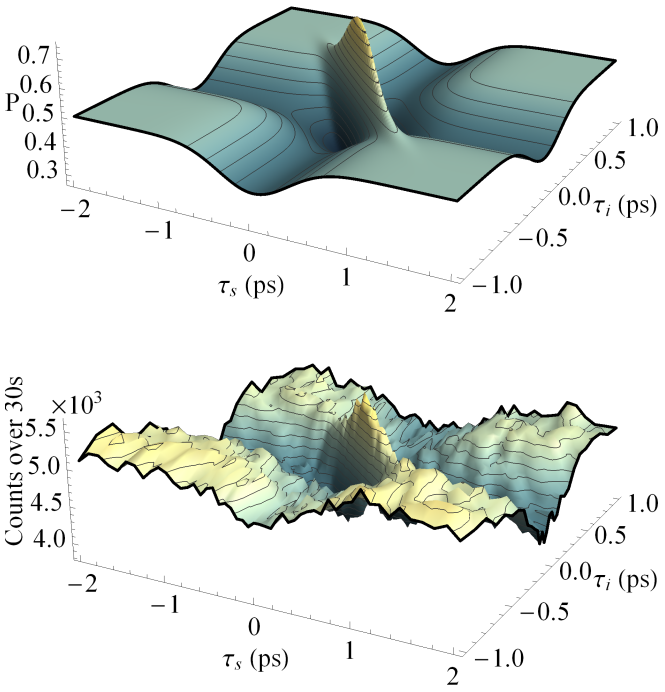

FIG. 12. Top: Simulation of Eq. (47) with experimental parameters. Bottom: experimental acquisition obtained by monitoring four-fold coincidences over 15 hours while scanning both τ_S and τ_I without spectral resolution of the herald.

$$P(\tau_S,\tau_I) = \frac{1}{4}\Bigg(1 + \left|\iint \mathrm{d}\omega\mathrm{d}\Omega\ |f(\omega,\Omega)|^2\, e^{i(\omega\tau_S+\Omega\tau_I)}\right|^2 - \iint \mathrm{d}^2\Omega\ |\rho_I(\Omega,\Omega')|^2\, e^{i(\Omega-\Omega')\tau_I} - \iint \mathrm{d}^2\omega\ |\rho_S(\omega,\omega')|^2\, e^{i(\omega-\omega')\tau_S}\Bigg), \tag{47}$$

which is similar to Eq.(41) with an additional dependence on τ_I. We simulated this expression using the Gaussian model in Fig. 12 and show the corresponding experimental result. It is straightforward to identify the three non-constant terms as familiar quantities. The second term is the cross-correlation between both JSA as a function of both delays. It can be written as the product of Fourier transform of the joint spectrum with respect to ω and Ω, thus reducing to the product of envelope functions centered at τ_S and τ_I. This term is responsible for the slanted peak in Fig. 12. The last two terms correspond respectively to the overlap integrals between the density matrices of the idlers and of the signals. They show the effect of interferences between uncorrelated photons and hence are visible as HOM dips along either τ_S or τ_I, as shown again in Fig. 12. This figure allows us to identify more clearly the range over which entanglement swapping can be verified, which is essentially the area over which the slanted peak appears, since the HOM dips correspond only to quantum interferences between unentangled single-photon states.

By exploring the range of both time delays in this configuration, we explicitly see the ultimate equivalence between signals and the idlers in what is effectively a four-photon interferometer. As such, it is adequate to consider $P_{jk}(\tau_S,\tau_I)$ and $P(\tau_S,\tau_I)$ as the most general representation of the phase-insensitive part of four-photon interference where TF entanglement is present.

V. CONCLUSION

In this work, we have undertaken a more thorough and more general analysis of the results we report on in Ref. [22]. In summary, we demonstrated and analyzed a novel scheme for TF entanglement swapping, using a multimode, spectrally-resolved Bell-state measurement as the heralding mechanism. The most salient feature of our method is the heralding of several, mutually-orthogonal Bell states derived from identical multimode entangled photon pairs. We further generalized our result to consider the case of non-zero time delay in the heralding Bell-state measurement, giving rise to Bell states with a varying amount of phase. Our setup is the first known to the authors to incorporate four simultaneous time-of-flight spectrometers, and thus points towards a promising venue of study of TF entangled four-photon interferometry.

As a proof-of-concept experiment, our work paves a way towards utilizing the high-dimensionality of the TF entanglement available in SPDC sources for distributed quantum information. It is straightforward to scale this protocol to herald a large number of orthogonal entangled states, which is in principle limited by the bandwidth, and thus the amount of the entanglement, of the SPDC sources. Our measurement scheme could further be extended to high-dimensional quantum teleportation and entanglement swapping, whereby ancillary photons and multiport beam splitters are used to implement a high-dimensional Bell state measurements, as has been recently demonstrated for path [23, 24] and orbital angular momentum [25] entanglement. Alternately, it is possible in principle to use sum-frequency generation to implement projective measurements onto high-dimensional TF-entangled states for the same purpose [26]. Finally, if used in combination with deterministic sources of entangled photon pairs [27] and with quantum memories [28], multimode quantum repeaters of the kind that our protocol allows could prove to be a scalable solution for multiplexed quantum networks.

ACKNOWLEDGEMENTS

The authors would like to thank M. Brown, A. O. C. Davis, and S. J. van Enk for valuable discussions. This project has received funding from the European Union's

Horizon 2020 research and innovation program under Grant Agreement No. 665148, and the National Science Foundation under Grant No. 1839216.

APPENDIX

Appendix A: Deriving the four-photon state

In the low gain regime, the output state of the n^{th} SPDC source, where $n \in \{1, 2\}$, is given by

$$|\psi_n\rangle = \sum_{p=0}^{\infty} \frac{\sqrt{\eta_n}^p}{p!} \left(\iint \mathrm{d}\omega_S \mathrm{d}\omega_I f_n(\omega_S, \omega_I) \hat{a}_n^\dagger(\omega_S) \hat{b}_n^\dagger(\omega_I) \right)^p |\text{vac}\rangle . \tag{A1}$$

The function $f_n(\omega_S, \omega_I)$ is the joint spectral amplitude (JSA), given by

$$f_n(\omega_S, \omega_I) = u_n(\omega_S + \omega_I) \text{sinc}\left[\frac{\Delta k_n(\omega_S, \omega_I) L}{2} \right], \tag{A2}$$

where u_n represents the spectral mode function of the pump, Δk_n is the wave-vector mismatch between the pump, signal and idler modes, and L is the length of the interaction medium. Finally, η_n is the gain of the parametric process, which depends on the length L, the non-linear strength of the material and the number of photons in the pump beam.

The SPDC state due to the two independent sources can be written as a tensor product $|\psi_1\rangle \otimes |\psi_2\rangle$. We expand this and keep only terms of order η, which are responsible for the four-photon contribution, obtaining the following state after normalization

$$|\psi_\eta\rangle = \frac{\left(\sqrt{\eta_1 \eta_2} \, |\psi_{12}\rangle + \frac{\eta_1}{2} |\psi_{11}\rangle + \frac{\eta_2}{2} |\psi_{22}\rangle \right)}{\sqrt{\eta_1 \eta_2 + \eta_1^2/4 + \eta_2^2/4}}, \tag{A3}$$

where

$$|\psi_{nm}\rangle = \int \mathrm{d}^4\omega \; f_n(\omega_S, \omega_I) f_m(\omega_S', \omega_I') \times \hat{a}_n^\dagger(\omega_S) \hat{a}_m^\dagger(\omega_S') \hat{b}_n^\dagger(\omega_I) \hat{b}_m^\dagger(\omega_I') \, |\text{vac}\rangle . \tag{A4}$$

is the four-photon state arising from either a photon pair from each source, or two pairs from one source and none from the other.

To facilitate the discussion of our results, we made a few simplifying assumptions in the main text, which we will now enumerate in the context of Eq. (A3). First, we assumed that both sources are identical, such that $f_1(\omega_S, \omega_I) = f_2(\omega_S, \omega_I) = f(\omega_S, \omega_I)$ and $\eta_1 = \eta_2 = \eta$. This is because in the experiment, the two sources are derived from double-pumping the same crystal as in Ref. [29], and are matched to a great degree as discussed in the experimental section. Further, any source mismatch does not reduce the quality of the entanglement in the swapped state, just the visibility of quantum interference in the method we use to verify entanglement.

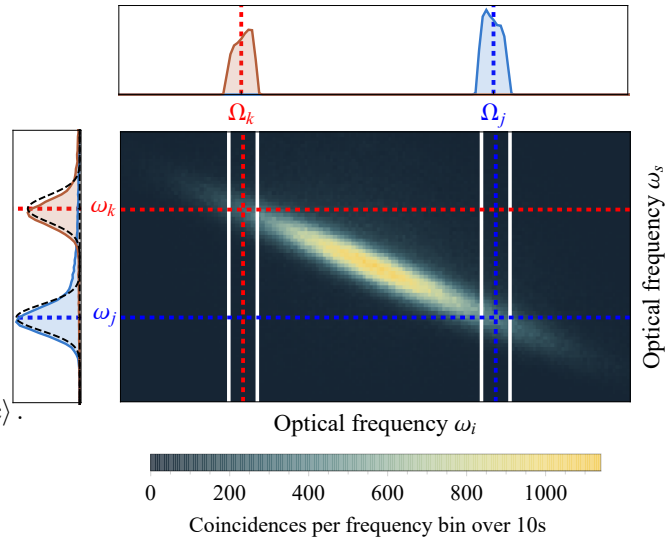

FIG. 13. Representation of the effect of finite resolution on the heralding. The finite bandwidth (white vertical lines) implies that a detection at frequencies (Ω_j, Ω_k) (vertical dashed lines) is integrated over the filtered modes, shown in the top plots. The heralded modes are represented on the left, where the black dashed line represent $|\phi_j|^2$ and $|\phi_k|^2$ from the pure state model.

Second, we assumed that the relative phases between the three terms in Eq. (A3) are random. This implies that these terms are not mutually coherent and therefore do not contribute to any quantum interference. In reality there is such a coherence, which is due to the phase of the pump, and we observe this in both two- and four-photon interference, as we show in Appendix D. However, this phase drifts over the course of the interference measurements we will describe, which are several hours long, and thus $|\psi_{11}\rangle$ and $|\psi_{22}\rangle$ contribute to a constant background in these measurements.

Finally, in the main text we focused our attention solely on the $|\psi_{12}\rangle$ term of Eq. (A3), which corresponds to each source producing a pair of entangled photons, which is rewritten as $|\psi\rangle$ for better readability. In most entanglement swapping and quantum teleportation experiments relying on SPDC sources, the other two terms (the double-pair terms), though present, do not contribute when the four photons are detected in coincidence, so that heralded states are *post-selected* [30]. Similarly, the double-pair terms only contribute in our setup in the aforementioned interference measurement, where they constitute a constant background, which we measure and subtract in Appendix F.

Appendix B: Mixed state model

In the realistic case, the BSM on the idler photons is not performed with perfect resolution, but rather within a finite spectral window. In our case, this is

due to the resolution of the time-of-flight spectrometer, which is a convolution of multiple response functions in the frequency-to-time conversion. It is dominated by the timing jitter ($\simeq 20$ ps) of the superconducting nanowires.When this resolution is not perfect, then we can show that the signal photons are heralded into a mixed state. The effect of this finite resolution on the heralded spectral distributions is shown graphically in Fig. 13.

We begin by redefining the BSM operator as:

$$\begin{aligned}\hat{\Pi}_{lm}^{\mathrm{BSM}} &= \iint \mathrm{d}\Omega_j \mathrm{d}\Omega_k |t_l(\Omega_j)|^2 |t_m(\Omega_k)|^2 \ \hat{\Pi}_{jk}^{\mathrm{BSM}} \\ &= \iint \mathrm{d}\Omega_j \mathrm{d}\Omega_k |t_l(\Omega_j)|^2 |t_m(\Omega_k)|^2 \left|\Omega_j, \Omega_k\right\rangle \left\langle \Omega_j, \Omega_k\right|, \\ \left|\Omega_j, \Omega_k\right\rangle &= \hat{b}_3^\dagger(\Omega_j)\hat{b}_4^\dagger(\Omega_k)\left|\mathrm{vac}\right\rangle,\end{aligned} \tag{B1}$$

where $t_{l(m)}(\Omega_{j(k)})$ are transmission amplitudes centered at $\Omega_{l(m)}$, and satisfy $\sum_{lm} |t_l(\Omega_j)|^2 |t_m(\Omega_k)|^2 = 1$. We have introduced new indices l, m, so that we may incorporate the j,k-dependent quantities from the main text into our analysis. Moreover, it is straightforward to show that the POVM element (3) is obtained by setting $t_{l(m)}(\Omega) \to \delta(\Omega - \Omega_{l(m)})$. To simplify our notation henceforth, we will use the following shorthand

$$\iint_{lm} \mathrm{d}\Omega_j \mathrm{d}\Omega_k := \iint \mathrm{d}\Omega_j \mathrm{d}\Omega_k |t_l(\Omega_j)|^2 |t_m(\Omega_k)|^2. \tag{B2}$$

It can be seen from Fig.5 that the finite resolution of the idler detection bin reduces the purity of the heralded signal state, due to the entanglement of the two-photon state. Because of this, the POVM element (B1) requires that we describe the heralded state as a mixed state

$$\hat{\rho}_{lm} = \frac{\mathrm{Tr}_{\hat{b}}\left[\hat{\Pi}_{lm}^{\mathrm{BSM}} \left|\psi_{12}\right\rangle \left\langle\psi_{12}\right|\right]}{p_{lm}}, \tag{B3}$$

where $\mathrm{Tr}_{\hat{b}}$ is the partial trace over the subspace defined by operators $\hat{b}_1$ and $\hat{b}_2$. Analogously to the pure state case, the probability p_{lm} are defined as

$$\begin{aligned} p_{lm} &= \mathrm{Tr}\left[\hat{\Pi}_{lm}^{\mathrm{BSM}} \left|\psi_{12}\right\rangle \left\langle\psi_{12}\right|\right] \\ &= \iint_{lm} \mathrm{d}\Omega_j \mathrm{d}\Omega_k \ p_{jk}. \end{aligned} \tag{B4}$$

where the idler density matrix is defined as Eq.(6), and we again obtain Eq.(7) by setting the filters $t_{l(m)}$ as δ functions.

We may now compute the heralded state density matrix:

$$\hat{\rho}_{lm} = \frac{1}{p_{lm}} \iint_{lm} \mathrm{d}\Omega_j \mathrm{d}\Omega_k \ p_{jk} \ \left|\Psi_{jk}\right\rangle \left\langle\Psi_{jk}\right| \tag{B5}$$

while recalling the definition of $\phi_{j(k)}(\omega)$ in $\left|\Psi_{jk}\right\rangle$ as

$$\phi_{j(k)}(\omega) = \frac{f(\omega, \Omega_{j(k)})}{\sqrt{\rho_{\mathrm{I}}(\Omega_{j(k)}, \Omega_{j(k)})}}. \tag{B6}$$

This has the intuitive interpretation of a mixed state as an incoherent sum of pure states over the detection bandwidth of $t_{l(m)}$. All of the measured quantities follow in a straightforward manner. In the absence of frequency resolution, we herald again the mixed state

$$\hat{\rho} = \sum_{lm} p_{lm} \ \hat{\rho}_{lm}, \tag{B7}$$

just as with the pure state model.

The heralded JSI is given by:

$$F_{lm}(\omega_1, \omega_2) = \left\langle \omega_1, \omega_2\right| \hat{\rho}_{lm} \left|\omega_1, \omega_2\right\rangle, \tag{B8}$$

which can be expressed in terms of F_{jk} as

$$F_{lm}(\omega_1, \omega_2) = \frac{1}{p_{lm}} \iint_{lm} \mathrm{d}\Omega_j \mathrm{d}\Omega_k \ p_{jk} \ F_{jk}(\omega_1, \omega_2). \tag{B9}$$

The integrated JSI corresponding to the state $\hat{\rho}$ is again given by

$$F(\omega_1, \omega_2) = \sum_{lm} p_{lm} F_{lm}(\omega_1, \omega_2). \tag{B10}$$

When the signal photons in the state $\hat{\rho}_{lm}$ are incident on a 50:50 beamsplitter, the coincidence fringes at the output are given by

$$P_{lm}(\tau_{\mathrm{S}}, \tau_{\mathrm{I}}) = \mathrm{Tr}\left(\hat{\Pi}_{\mathrm{verif}} \hat{\rho}_{lm}\right) = \iint \mathrm{d}^2\omega \left\langle \omega, \omega'\right| \hat{\rho}_{lm} \left|\omega, \omega'\right\rangle, \tag{B11}$$

where $\left|\omega, \omega'\right\rangle = \hat{a}_3^\dagger(\omega)\hat{a}_4^\dagger(\omega')\left|\mathrm{vac}\right\rangle$ as before. Evaluating this in terms of P_{jk}, we

$$P_{lm}(\tau_{\mathrm{S}}, \tau_{\mathrm{I}}) = \frac{1}{p_{lm}} \iint_{lm} \mathrm{d}\Omega_j \mathrm{d}\Omega_k \ p_{jk} \ P_{jk}(\tau_{\mathrm{S}}, \tau_{\mathrm{I}}). \tag{B12}$$

Finally the integrated interference peak for the state $\hat{\rho}$ is recovered by taking

$$P(\tau_{\mathrm{S}}, \tau_{\mathrm{I}}) = \sum_{lm} p_{lm} \ P_{lm}(\tau_{\mathrm{S}}, \tau_{\mathrm{I}}). \tag{B13}$$

We will make a few comments regarding the most interesting feature of comparing this model with the pure state model. To this end, we shall represent the pure state $\left|\Psi_{jk}\right\rangle \left\langle\Psi_{jk}\right|$ as a density matrix in the $\{\left|\phi_j\right\rangle \left|\phi_k\right\rangle, \left|\phi_k\right\rangle \left|\phi_j\right\rangle\}$ basis as follows:

$$\left|\Psi_{jk}\right\rangle \left\langle\Psi_{jk}\right| = \frac{1}{2\mathcal{C}_{jk}} \begin{pmatrix} 1 & e^{i\theta_{jk}} \\ -e^{-i\theta_{jk}} & 1 \end{pmatrix}. \tag{B14}$$

Meanwhile, the mixed state $\hat{\rho}_{lm}$ has the representation:

$$\hat{\rho}_{lm} = \frac{1}{p_{lm}} \iint_{lm} \mathrm{d}\Omega_j \mathrm{d}\Omega_k \ \frac{p_{jk}}{2\mathcal{C}_{jk}} \begin{pmatrix} 1 & e^{i\theta_{jk}} \\ -e^{-i\theta_{jk}} & 1 \end{pmatrix}. \tag{B15}$$

Notably, the off-diagonal terms $e^{\pm i\theta_{jk}} = e^{\pm i(\Omega_j - \Omega_k)\tau_{\mathrm{I}}}$, the coherence terms, are the hallmark of the bipartite

entanglement in these states, and are responsible for the interference we observe in P_{jk}. It seems reasonable then to ask if, and to what extent, the averaging over the l, m bands in the mixed state is expected to reduce the entanglement. Take first the special case of $\tau_{\mathrm{I}} = 0$. In this case, $\theta_{jk} = 0 \; \forall \; j, k$, and the off-diagonal terms are equal to unity, and hence, no phase-averaging occurs for the mixed state $\hat{\rho}_{lm}$. Indeed, the off-diagonals survive even for the fully-averaged state $\hat{\rho}$, and one can interpret this as the reason why the interference peak survives at full visibility for $\tau_{\mathrm{I}} = 0$.

More generally, however, for $\tau_{\mathrm{I}} \neq 0$, the disagreement between the two models becomes more salient. The pure-state model assumes that the idler photons are detected at monochromatic frequency modes at (Ω_j, Ω_k), which are necessarily infinite in extent in the time domain. This means that the idler photons remain indistinguishable at the output of the BSM beamsplitter, even for arbitrary τ_{I} delays at the input. On the other hand, taking into account the averaging over the l, m bands introduces distinguishability, and the BSM is no longer ideal in this case. Furthermore, this averaging introduces more distinguishability the larger τ_{I} is, since the argument of the phase factor $(\Omega_j - \Omega_k)\tau_{\mathrm{I}}$ is proportional to this time delay. This phase-averaging results in a reduction of the off-diagonal terms, and of the visibility of the P_{lm} interference for large enough τ_{I}. This behavior is most clearly seen in the profile of the fully-integrated two-dimensional peak in Fig. 12, which results from averaging over all phases with a weight p_{jk}. The peak vanishes in the τ_{I} direction over a delay timescale comparable to the inverse bandwidth of the idler photons. The intuitive interpretation is that the idler photons become distinguishable at the output of the beamsplitter when the relative delay is at least as long as their pulse durations.

Appendix C: Time-of-flight spectrometers calibration

To ensure that our TOFS are accurate, it is necessary to calibrate them. While it is usually sufficient to use a rough estimate of the dispersion imprinted by the fiber spool or by the CFBG, this doesn't take into account waveguide dispersion or other sources of dispersion in the setup. Therefore, we opted for an in-situ calibration utilizing the single photons from the SPDC.

We used a pulse shaper based on a spatial light modulator (SLM) placed at the midpoint of a 4-f line [31], enabling us to address both the amplitude and phase of the mode-function of single photons over a 30 nm range with a resolution of 0.02 nm. By scanning a narrow interference filter of 1 nm FWHM over the SLM mask while recording the resulting time tags, we obtain a calibration curve between the recorded time tags and the wavelength of the filter set on the pulse shaper. Over our wavelength range, this function is mostly linear and its slope is the dispersion parameter of the TOFS. The results are shown in Fig. 14. With the two CFBG-based spectrometers, we obtained a dispersion of 944±4 ps/nm and 946±2 ps/nm. With the fiber spools, we measured an equal dispersion of -54 ± 1 ps/nm. With the calibration in hand, it is straightforward to convert time stamps to wavelength for any detection event after a TOFS, see for example Fig.3.

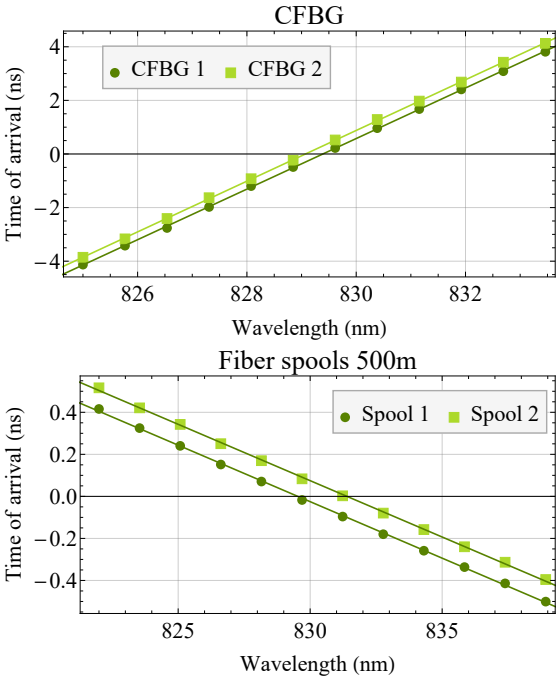

FIG. 14. Calibration of each TOFS. The curves have been offset vertically for better visibility.

Appendix D: Source distinguishability

The entanglement verification protocol we use, that is, the two-photon interference of the state $|\Psi_{jk}\rangle$, ultimately relies on the indistinguishability of the two source states. To see this, we relabel the source JSA's as $f_1(\omega, \Omega)$ and $f_2(\omega, \Omega)$, and for simplicity, we assume that they are identical up to a translation in frequency space. Note now that this leads to a heralded state

$$|\Psi_{jk}\rangle \propto |\phi_j^1\rangle_1 |\phi_k^2\rangle_2 - |\phi_k^1\rangle_1 |\phi_j^2\rangle_2 \,, \tag{D1}$$

where

$$|\phi_{j(k)}^{1(2)}\rangle = \int \mathrm{d}\omega \phi_{j(k)}^{1(2)}(\omega) \hat{a}_{1(2)}^{\dagger}(\omega) |\mathrm{vac}\rangle \,, \tag{D2}$$

and

$$\phi_{j(k)}^{1(2)}(\omega) = \frac{f_{1(2)}(\omega, \Omega_{j(k)})}{\rho_{1(2)}(\Omega_{j(k)}, \Omega_{j(k)})}. \tag{D3}$$

Although this state is still entangled, the verification method using coincidence fringes in $P_{jk}(\tau_{\mathrm{S}})$ will suffer

from a reduction in visibility due to the distinguishability of f_1 and f_2. To see this, we recalculate $P_{jk}(\tau_S)$ in its approximate form (45), and find

$$P_{jk}(\tau_S) \approx \frac{1}{2}\left(1 - V_{jk}\, e^{\sigma_S^2\tau_S^2} \cos\left[\left(\frac{\omega_j^1+\omega_j^2}{2} - \frac{\omega_k^1+\omega_k^2}{2}\right)\tau_S\right]\right) \tag{D4}$$

where the visibility V_{jk} is given by

$$V_{jk} = \left(\int \mathrm{d}\omega \phi_j^{1*}(\omega)\phi_j^2(\omega)\right)\left(\int \mathrm{d}\omega \phi_k^{1*}(\omega)\phi_k^2(\omega)\right). \tag{D5}$$

We can maximize this visibility by maximizing the overlap f_1 and f_2. We see that this latter provides a lower bound on V_{jk} by writing

$$\begin{aligned}\int \mathrm{d}\omega \phi_j^{1*}(\omega)\phi_j^2(\omega) &= \frac{\int \mathrm{d}\omega f_1^*(\omega,\Omega_j) f_2(\omega,\Omega_j)}{\sqrt{\rho_1(\Omega_j,\Omega_j)\rho_2(\Omega_j,\Omega_j)}} \\ &\geq \int \mathrm{d}\omega \mathrm{d}\Omega f_1^*(\omega,\Omega) f_2(\omega,\Omega),\end{aligned} \tag{D6}$$

and likewise for k.

It is relatively straightforward to maximize the quantity on the left by tuning experimental parameters, namely pump wavelength, phasematching angle, and transverse optical fiber position (due to residual spatial chirp), and observing two-fold coincidences resulting from first order interference of the sources. Because both sources are pumped with the same pulse, the two-photon term of the state is given by

$$\begin{aligned}|\psi\rangle \propto \int \mathrm{d}\omega \mathrm{d}\Omega \Big(& f_1(\omega,\Omega)\hat{a}_1^\dagger(\omega)\hat{b}_1^\dagger(\Omega) + \\ & f_2(\omega,\Omega)\hat{a}_2^\dagger(\omega)\hat{b}_2^\dagger(\Omega)\Big)|\mathrm{vac}\rangle\,.\end{aligned} \tag{D7}$$

A straightforward calculation shows that the probability of a two-fold coincidence between ports $\hat{b}_3$ (or $\hat{b}_4$) and $\hat{a}_3$ (or $\hat{a}_4$) is given by

$$\begin{aligned}P_{cc} &= \frac{1}{4}\int \mathrm{d}^2\omega \Big| f_1(\omega,\Omega) \pm f_2(\omega,\Omega)\Big|^2 \\ &= \frac{1}{2}\Big(1 \pm \mathrm{Re}\int \mathrm{d}^2\omega f_1^*(\omega,\Omega) f_2(\omega,\Omega)\Big)\end{aligned} \tag{D8}$$

In the following, we will outline additional measurements to quantify the source indistinguishability. In our case, our dual-pass geometry implies that we need to match the JSI of both sources, which is achieved when both signals and idlers from both sources have maximum overlap. We opted for a bulk crystal source in Type II to enable pumping in both directions while being able to separate our four photons into different paths. We used a BiBO crystal due to its relatively high non linearity.

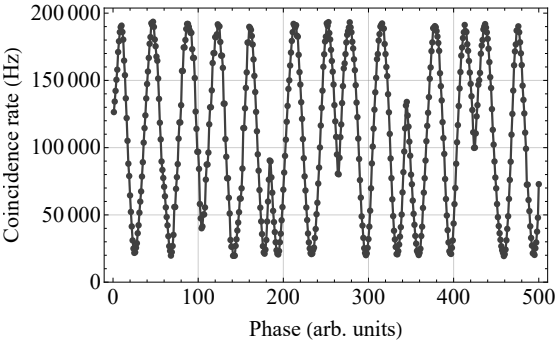

FIG. 15. Measured coincidence fringes $P_{cc}(\tau)$ with a contrast of 80%.

First, we measured the JSI by directing the two photons from either source into the fiber spools, since their large spectral bandwidth would be cropped with the CFBG. The JSI from each source is depicted in Fig4. They show that both sources are nearly indistinguishable; a singular value decomposition yields a Schmidt number of $K_1 = 2.9 \pm .1$ and $K_2 = 2.9 \pm .1$. These values are lower than the theoretical expectation ($K \sim 5$) because of the timing jitter of our detectors that result in a broader distribution. This was confirmed by measuring the JSI with the CFBG's, which have a better resolution but are limited in range. The correlation width was found to be lower and therefore the Schmidt number can be expected to be at least $K = 4$.

Note that this method is insensitive to any spectral phase difference, such as dispersion from the pump (which is equivalent to setting $\alpha \in \mathbb{C}$ in the JSA (28)), since the second pump is slightly more dispersed than the first due to propagation. This has been shown to increase the entanglement and the Schmidt number [7, 32]. However, this difference should be negligible, and the method presented that relies on Eq.(D8) allows for a more accurate estimation of the overlap. Nevertheless, the JSI measurement showed near-perfect correspondence between the intensity of the two sources which is a critical step to ensure indistinguishably between the uncorrelated photon pairs.

To further characterize the indistinguishability of the sources, we measure their heralded $g^{(2)}$ by splitting their signal photon into a beamsplitter. This yields a value of $g_1^{(2)} = 0.16 \pm 0.003$ and $g_2^{(2)} = 0.14 \pm 0.003$. These values are consistent with the relatively high optical power that is utilized to pump the sources in order to maximize the probability of four-fold coincidences. The lower value of $g^{(2)}$ for source 2 is consistent with the fact that it also has a higher heralding efficiency than source 1. The reason is not entirely clear, but it is likely that the previous interaction with the PDC crystal on the first pass results in an additional filtering on the pump as well as a slight reduction in optical power because of absorption.

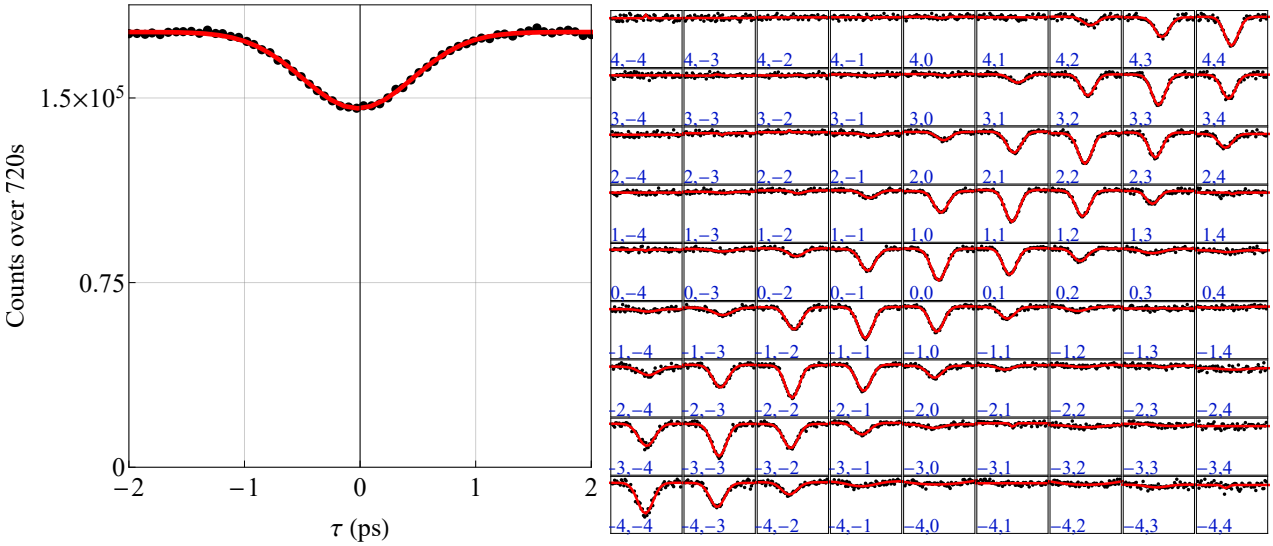

FIG. 16. Left: HOM dip between the signal photons heralded by a coincidence between the idler photons. Right: same measurement but with spectral resolution of the heralding photons, labelled j,k for Ω_k,Ω_k, where index $j,k=0$ corresponds to the center frequency ω_0. The labelling convention is described in Fig. 3.

Finally, in Fig. 15 we measured the coincidences between ports $\hat{b}_3$ and $\hat{a}_3$ (see Fig1) while scanning the relative phase between the two pump fields with a piezoelectric stack, which is related to the probability from Eq.(D8). We scanned using a slow voltage ramp resulting in a few micrometers of displacement over a few seconds. The visibility of those fringes is 80%, which is a direct measurement of the overlap between the two sources, and therefore a quantification of distinguishability.

Appendix E: Purity of the heralded states

Since the state $|\psi_{12}\rangle$ from the sources is assumed to be a pure state, the purity of the heralded states $|\Psi_{jk}\rangle$ is ultimately dependent on the amount of spectral filtering in the heralding BSM. To assess this purity, we measure HOM interference between the heralded signal photons when there is no beamsplitter in the idler arms. In this case, upon a coincidence detection of the idler photons at (Ω_j,Ω_k), the reduced state of the signal photons is separable, and given by

$$\hat{\rho}_j\otimes\hat{\rho}_k=\left(\int \mathrm{d}^2\omega\rho_j(\omega,\omega')\right)\left(\int \mathrm{d}^2\tilde{\omega}\rho_k(\tilde{\omega},\tilde{\omega}')\right)\hat{a}_1^\dagger(\omega)\hat{a}_2^\dagger(\tilde{\omega})\,|\mathrm{vac}\rangle\,\langle\mathrm{vac}|\,\hat{a}_1(\omega')\hat{a}_2(\tilde{\omega}'),\quad \text{(E1)}$$

where

$$\rho_{j(k)}(\omega,\omega')=\int \mathrm{d}\Omega|t_{j(k)}(\Omega)|^2 f(\omega,\Omega)f^*(\omega',\Omega).\quad \text{(E2)}$$

When the signal photons in this state are incident on a 50:50 beamsplitter, the expected visibility of the HOM interference is given by [33]

$$V=\mathrm{Tr}(\hat{\rho}_j\hat{\rho}_k),\quad \text{(E3)}$$

and when the idlers are detected in identical frequency bins $(j=k)$, this becomes

$$V=\mathrm{Tr}(\hat{\rho}^2_{j(k)})=\mathcal{P}(\hat{\rho}_{j(k)}),\quad \text{(E4)}$$

where $\mathcal{P}(\cdot)$ denotes the purity of a state. Thus, for $(j=k)$ the visibility of the HOM dip gives a lower bound on the purity of the state $\hat{\rho}_{j(k)}$, and by extension, the state $\hat{\rho}_{jk}$. Our measurements, shown in Fig. 16, indicate that purity of the heralded states is *at least* 70%, as evidenced by the HOM visibility along the $j=k$ line. By comparison, a direct calculation of the expected purity using our experimental parameters gives $\sim 78\%$. The purity of our heralded state seems to be dominated by the spectral resolution of our spectrometer. Without spectral resolution, the purity of the heralded state is about 20% as shown in Fig. 16. We note that at the time of writing, an experiment has been reported using spectral-to-spatial spectrally-multiplexed HOM interference scheme, showing a similar decrease in HOM visibility as a function of distance between frequency bins [34].

Appendix F: Background signal

As shown by Eq.(A3), the full four photon state in the interferometer (see Fig. 1) contains a contribution from photon pairs emitted by individual sources due to the stochastic nature of parametric down conversion. These terms contribute to $P(\tau_S)$ in the form of interferences that get averaged over the course of a measurement. It is

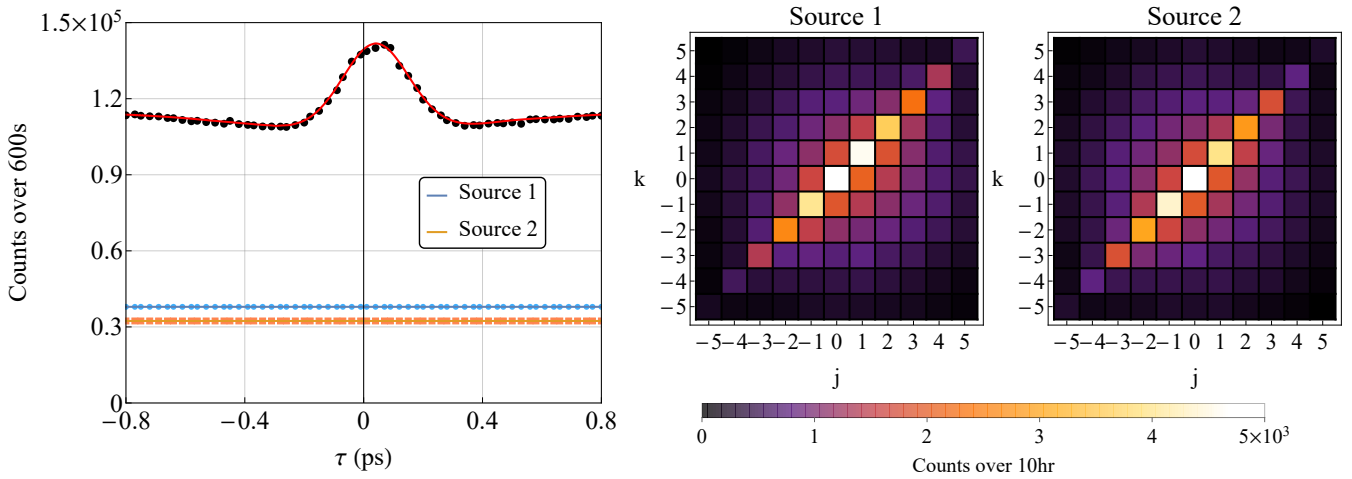

FIG. 17. Left: $P(\tau_S)$ without removing the constant two photon contribution from source 1 (dot) and source 2 (square). $P(\tau_S)$ resembles Eq.(41) and the fit is obtained by summing the individual fits of P_{jk} as given by (26). Right: distribution of these background terms as a function of the heralding frequencies Ω_j, Ω_k

therefore possible to remove that contribution from the signal subsequently to the measurement by blocking a source and recording the rate of four-fold coincidences.

We therefore repeated the measurement of $P_{jk}(\tau_S)$ with either source blocked to obtain the constant background signal for each j,k frequencies, as shown in Fig. 17. This shown that the background terms are similar between both sources, therefore the two sources are similar. Summing over all the bins, we can plot on the same scale the contribution of all term in Fig. 17. The peak corresponds to interferences from $|\psi_{12}\rangle$ while the flat terms represent $|\psi_{11}\rangle$ and $|\psi_{22}\rangle$. As expected from the theory, both source contribute to 1/4 of the full signal. Removing those backgrounds at Ω_j, Ω_k from P_{jk}, we obtain the fringes from the main paper with optimal visibility.

As stated in the main text, we have assumed that the three terms in the full state Eq. (A3) are mutually incoherent. This is because our measurements are taken over a long timescale of a few hours where the optical phase drifts significantly and any phase-sensitive interference can be neglected. Over a shorter time-scale, we can measure this optical phase in real time by measuring fourfold coincidences with the two beamsplitters present, while scanning the PZT between both sources. A straightforward calculation taking into account the full state (A3) shows that there is a term that oscillates at the sum frequency $\omega+\Omega \approx \omega_p$, where ω_p is the pump frequency, corresponding to about 415 nm in wavelength. In Fig. 18, we plot the measured interference of the two-fold (red) coincidences against the four-fold fringes (blue), where the latter can be seen to modulate at twice the frequency of the two-fold modulation.

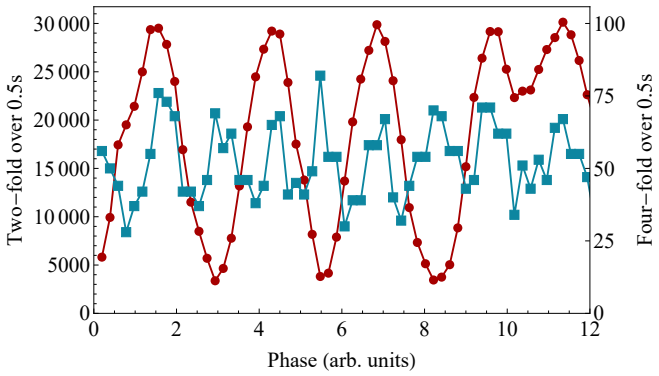

FIG. 18. Interference fringes in the two-fold (red) and fourfold (blue) coincidences, obtained in "real-time", while scanning a PZT as described in the text. The four-fold fringes can be seen to occur at twice the frequency of the two-fold fringes.

Appendix G: Orthogonal modes

From Eq.(9), we see that the heralded state $|\Psi_{jk}\rangle$ is dependent on the modes $|\phi_j\rangle$ and $|\phi_k\rangle$, which, in the pure state case, results in a heralded joint spectrum (17) dependent on the outer products $\phi_j(\omega_1)\phi_k(\omega_2)$. For each heralding bin j and k, we label the heralded JSI from (9) as $F_n(\omega_1,\omega_2)$, where n indexes a pair (j,k). These are normalized as $\int \mathrm{d}^2\omega F_n(\omega_1,\omega_2) = 1\ \forall\ n$ but are not orthogonal, even in the pure state case, *i.e* $\int \mathrm{d}^2\omega F_n(\omega_1,\omega_2)F_m(\omega_1,\omega_2) \neq \delta_{nm}$. Orthogonality is usually a corner stone in any quantum protocol, and it is therefore necessary to select the heralded states from our measurement that are orthogonal. To do so, we utilize our measurement of F_{jk} by measuring the spectral coincidences between the signal's photon heralded by a BSM on the idlers. We then obtain the set of JSI presented in Fig. 7(b).

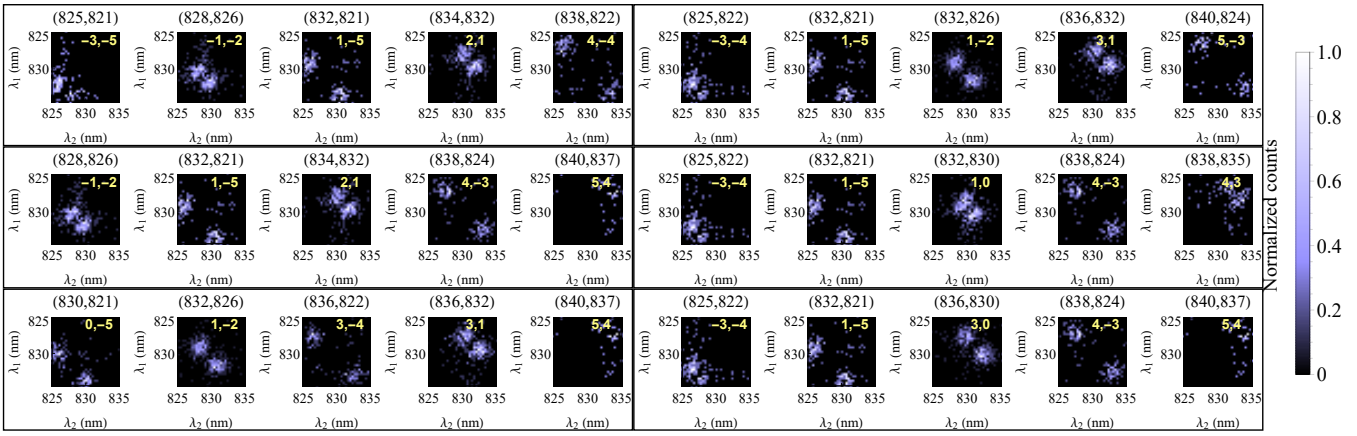

FIG. 19. Sets of orthogonal modes F_{jk} that have less than 15 % of mutual overlap. The insets label j and k.

First, it is important to notice the symmetry in (9), where $F_{jk} = F_{kj}$ for $j \neq k$. Since our TOFS are well-calibrated, it is reasonable to symmetrize our measured heralded JSI by averaging the experimentally obtained F_{jk} and F_{kj} (for $j \neq k$) thus defining the F_n functions. Then we compute the mutual overlaps $\int \mathrm{d}^2\omega F_n(\omega_1,\omega_2)F_m(\omega_1,\omega_2)$ and use an algorithm to select a set of modes $\{F_n\}$ which all have an overlap below a certain threshold of 15%. We represented a few of these JSI in Fig. 19. Since the spectral range of our high resolution TOFS is limited, so is the range over which we can compute overlap, as can be seen from the modes that are labelled with a large j,k. Nevertheless, there is a sufficient amount of spectral coincidence in those cases to infer orthogonality with the other JSI.

Note that while this overlap is computed between the joint spectral intensities and not between the states, it can be shown that if the overlap in intensity is zero, then the states are necessarily orthogonal, hence the strategy is valid to select which $|\Psi_{jk}\rangle$ are mutually orthogonal. Therefore, it is fair to say that the JSI's F_{jk} from Fig. 19 correspond to heralded states $|\Psi_{jk}\rangle$ that are all mutually orthogonal.

Appendix H: Miscellaneous functions and relations

Our theoretical derivation relies on the definition of the $\phi_{j(k)}(\omega)$ functions which renders computation easier thanks to the Gaussian approximation. These functions can be also written in a density matrix formalism.
Using the definitions from Sec.II, the $\phi_{j(k)}$ functions are defined from the JSA by:

$$f(\omega,\Omega_{j(k)}) = \sqrt{N_j}\phi_{j(k)}(\omega), \tag{H1}$$

where N_j is a function that depends on the heralding frequency Ω_j, the JSA bandwidth over the idler axis σ_I and the amount of entanglement α. The reduced density matrix of the idler, given by Eq.(30), can then be written in the following manner:

$$\begin{aligned}\rho_\mathrm{I}(\Omega_j,\Omega_k) &= \int \mathrm{d}\omega\ f(\omega,\Omega_j)f^*(\omega,\Omega_k)\\ &= \sqrt{N_jN_k}\int \mathrm{d}\omega\ \phi_j(\omega)\phi_k^*(\omega)\\ &= \sqrt{N_jN_k}\,\langle\phi_j|\phi_k\rangle\,,\end{aligned} \tag{H2}$$

where we see that the idler density matrix can be linked to the overlap integral between the heralded signal states. The $N_{j(k)}$ functions are then found to be equal to the diagonal elements of the idlers density matrix:

$$N_{j(k)} = \rho_\mathrm{I}\left(\Omega_{j(k)},\Omega_{j(k)}\right), \tag{H3}$$

since the $\phi_{j(k)}$ are ℓ^2 normalized.

The signal density matrices then follow a similar derivation, with

$$\begin{aligned}\rho_\mathrm{S}(\omega,\omega') &= \int \mathrm{d}\Omega_{j(k)}\ f(\omega,\Omega_{j(k)})f^*(\omega',\Omega_{j(k)})\\ &= \int \mathrm{d}\Omega_{j(k)}\ N_{j(k)}\phi_{j(k)}(\omega)\phi_{j(k)}^*(\omega),\end{aligned} \tag{H4}$$

and the diagonal elements are given by

$$\rho_\mathrm{S}(\omega,\omega) = \int \mathrm{d}\Omega_{j(k)}\ N_{j(k)}\left|\phi_{j(k)}(\omega)\right|^2. \tag{H5}$$

It is easy to show that in the case of similar sources, we also have the identity

$$\rho_\mathrm{S}(\omega,\omega') = \rho_\mathrm{S}^*(\omega',\omega). \tag{H6}$$

Finally, the overlap between the modes ϕ_j and ϕ_k can also be written in term of the density matrices, as:

$$\langle\phi_j|\phi_k\rangle = \frac{\rho_\mathrm{I}(\Omega_j,\Omega_k)}{\sqrt{N_jN_k}} \tag{H7}$$

[1] H. J. Kimble, Nature **453**, 1023 (2008).
[2] B. Brecht, D. V. Reddy, C. Silberhorn, and M. G. Raymer, Physical Review X **5**, 041017 (2015).
[3] R. Jozsa and N. Linden, Proceedings of the Royal Society of London. Series A: Mathematical, Physical and Engineering Sciences **459**, 2011 (2003).
[4] A. K. Ekert, Phys. Rev. Lett. **67**, 661 (1991).
[5] H. de Riedmatten, I. Marcikic, J. A. W. van Houwelingen, W. Tittel, H. Zbinden, and N. Gisin, Phys. Rev. A **71**, 050302(R) (2005).
[6] M. G. Raymer, A. H. Marcus, J. R. Widom, and D. L. Vitullo, Journal of Physical Chemistry B **117**, 15559 (2013).
[7] V. Ansari, J. M. Donohue, B. Brecht, and C. Silberhorn, Optica **5**, 534 (2018), 1803.04316.
[8] T. Vértesi and M. Navascués, Phys. Rev. A **83**, 062112 (2011).
[9] C. H. Bennett, G. Brassard, C. Crépeau, R. Jozsa, A. Peres, and W. K. Wootters, Phys. Rev. Lett. **70**, 1895 (1993).
[10] M. Żukowski, A. Zeilinger, M. A. Horne, and A. K. Ekert, Phys. Rev. Lett. **71**, 4287 (1993).
[11] F. Graffitti, P. Barrow, A. Pickston, A. M. Brańczyk, and A. Fedrizzi, Phys. Rev. Lett. **124**, 053603 (2020).
[12] K. J. Blow, R. Loudon, S. J. D. Phoenix, and T. J. Shepherd, Phys. Rev. A **42**, 4102 (1990).
[13] S. Ramelow, L. Ratschbacher, A. Fedrizzi, N. K. Langford, and A. Zeilinger, Physical Review Letters **103**, 253601 (2009).
[14] A. Fedrizzi, T. Herbst, M. Aspelmeyer, M. Barbieri, T. Jennewein, and A. Zeilinger, New Journal of Physics **11**, 103052 (2009).
[15] N. Treps, V. Delaubert, A. Maître, J. M. Courty, and C. Fabre, Phys. Rev. A **71**, 013820 (2005).
[16] J. Roslund, R. M. De Araujo, S. Jiang, C. Fabre, and N. Treps, Nature Photonics **8**, 109 (2014).
[17] V. Thiel, J. Roslund, P. Jian, C. Fabre, and N. Treps, Quantum Science and Technology **2**, 034008 (2017).
[18] V. Torres-Company, J. Lancis, and P. Andres, Progress in Optics **56**, 1 (2011).
[19] K. Goda and B. Jalali, Nature Photonics **7**, 102 (2013).
[20] A. O. C. Davis, P. M. Saulnier, M. Karpiński, and B. J. Smith, Opt. Express **25**, 12804 (2017).
[21] H. Kim, S. M. Lee, and H. S. Moon, Scientific reports **5**, 1 (2015).
[22] S. Merkouche, V. Thiel, A. Davis, , and B. Smith, (2021), in preparation.
[23] Y.-H. Luo, H.-S. Zhong, M. Erhard, X.-L. Wang, L.-C. Peng, M. Krenn, X. Jiang, L. Li, N.-L. Liu, C.-Y. Lu, A. Zeilinger, and J.-W. Pan, Phys. Rev. Lett. **123**, 070505 (2019).
[24] X.-M. Hu, C. Zhang, B.-H. Liu, Y. Cai, X.-J. Ye, Y. Guo, W.-B. Xing, C.-X. Huang, Y.-F. Huang, C.-F. Li, and G.-C. Guo, Phys. Rev. Lett. **125**, 230501 (2020).
[25] M. Erhard, M. Malik, M. Krenn, and A. Zeilinger, Nature Photonics **12**, 759 (2018).
[26] S. Merkouche, V. Thiel, and B. J. Smith, Phys. Rev. A **103**, 043711 (2021).
[27] L. Ginés, C. Pepe, J. Gonzales, N. Gregersen, S. Höfling, C. Schneider, and A. Predojević, Opt. Express **29**, 4174 (2021).
[28] M. Afzelius, C. Simon, H. de Riedmatten, and N. Gisin, Phys. Rev. A **79**, 052329 (2009).
[29] J.-W. Pan, D. Bouwmeester, H. Weinfurter, and A. Zeilinger, Physical Review Letters **80**, 3891 (1998).
[30] C. Wagenknecht, C.-M. Li, A. Reingruber, X.-H. Bao, A. Goebel, Y.-A. Chen, Q. Zhang, K. Chen, and J.-W. Pan, Nature Photonics **4**, 549 (2010).
[31] A. M. Weiner, Optics Communications **284**, 3669 (2011).
[32] A. O. C. Davis, V. Thiel, and B. J. Smith, Optica **7**, 1317 (2020).
[33] P. J. Mosley, J. S. Lundeen, B. J. Smith, P. Wasylczyk, A. B. U'Ren, C. Silberhorn, and I. A. Walmsley, Phys. Rev. Lett. **100**, 133601 (2008).
[34] O. Pietx-Casas, G. C. do Amaral, T. Chakraborty, R. Berrevoets, T. Middelburg, J. A. Slater, and W. Tittel, "Spectrally multiplexed hong-ou-mandel interference," (2021), arXiv:2111.13610 [quant-ph].